

CONSTRUCTION AND INSTRUMENTATION OF FULL-SCALE GEOGRID REINFORCED PAVEMENT TEST SECTIONS

**National Pooled Fund Study TPF-5(010)
Structural Improvement of Flexible Pavements Using Geosynthetics for Base Course
Reinforcements**

by

Karen S. Henry, Ph.D., P.E. ⁽¹⁾

Edel R. Cortez, Ph.D., P.E. ⁽¹⁾

Larry Danyluk ⁽¹⁾

Gregory Brentrup ⁽¹⁾

Nathan Lamie ⁽¹⁾

Troy Arnold ⁽¹⁾

¹ U.S. Army Corps of Engineers, Engineer Research and Development Center
Cold Regions Research and Engineering Laboratory
72 Lyme Road,
Hanover, New Hampshire 03755, United States

EXECUTIVE SUMMARY

A national pooled-fund study with the Federal Highway Administration (FHWA), including nine states, the University of Maine, and the U.S. Army Corps of Engineers Engineer Research and Development Center's Cold Regions Research and Engineering Laboratory (ERDC-CRREL) was conducted to assess the benefits of geogrid base course reinforcement in flexible pavements representative of major highways. Previous research regarding geogrid reinforcement of pavement base layers has involved thin asphalt concrete, thin or moderate base course thickness, and very weak subgrades—conditions not typical of major highway construction. This report documents the construction and instrumentation of a set of full-scale pavement test sections located in the Frost Effects Research Facility (FERF) at ERDC-CRREL.

To simulate traffic conditions of a typical highway, the experimental design was based on a pavement design life of 3×10^6 equivalent single axle loads (ESALs). Based on the 1993 AASHTO design guide for a subgrade of resilient modulus of 34.5 MPa (5 ksi), 610 mm (24 in) of base, 152 mm (6 in) of asphalt is required. The experimental design for this project included two asphalt concrete and two base course thicknesses. Two test sections were constructed for each combination of asphalt and base thickness: one with geogrid reinforcement and one without geogrid. The geogrid is located at the base course/ subgrade interface. Thus, there are eight test sections (2^3 factorial design). The thicknesses of the base course were 0.30 m (1 ft) and 0.61 m (2 ft). The asphalt concrete thicknesses were 102 mm (4 in) and 152 mm (6 in). The geogrid used in these experiments was Tensar BX1200. The test sections are instrumented with sensors to measure stress, strain, moisture and temperature at critical locations. The experimental design allows for systematic comparison of the influences of base thickness, asphalt thickness and geogrid presence.

The test sections were constructed indoors in the FERF, which has moisture and temperature controls. During construction of the test sections the temperature inside the FERF building was kept at approximately 23°C (73°F). The subgrade soil in the test sections was classified as AASHTO type A-4 (USCS type ML). It was placed at near optimum moisture content and maximum dry density. The as-built subgrade modulus values determined by falling weight deflectometer (FWD) tests ranged from approximately 55.2 to 75.8 MPa (8-11 ksi). The lower modulus values were produced by adding water to the top of the subgrade after paving. This process took about 5 months. During this time water was added in measured increments while periodically monitoring with a FWD and embedded moisture content sensors. At a depth of 2.44 m (8 ft) from the pavement surface and below the subgrade soil, there was a concrete floor that simulated natural bed rock.

Subsequent publications will present the accelerated traffic tests, the pavement response in terms of stress and strain, and the pavement performance in terms of permanent deformation and other forms of distress that may be observed. Analyses of the test results will provide an evaluation of the effects of geogrid reinforcement, and the basis for the development of pavement models compatible with future modifications to NCHRP 1-37A, Guide for Mechanistic-Empirical Design of New and Rehabilitated Pavement Structures, currently available from <http://www.trb.org/mepdg/>.

INTRODUCTION

The use of geogrids for reinforcement of pavements has been reported in the literature indicating varying degrees of success. Generally, the reported applications and experiments have been of limited scope, and most previous research pertaining to geogrids in pavements has involved thin asphalt concrete, thin or moderate base course thickness, and soft subgrades (California Bearing Ratio values of 3 or less)—e.g., the summary of 15-years of geosynthetic-reinforced base research provided by Perkins and Ismeik (1997), also Vischer (2003) and Perkins and Cortez (2005). In one study, Perkins (1999) found that geosynthetic reinforcement of test sections with 75 mm (3 in) of asphalt overlying 200-375 mm (8-14.5 in) of base provided significant benefit when the subgrade had a CBR of 1.5, but no improvement was noted when the subgrade had a CBR of 20.

A United States Federal Highway Administration (FHWA), pooled-fund study, TPF-5(010), entitled ‘Structural Improvement of Flexible Pavements Using Geosynthetics for Base Course Reinforcements,’ with participation of nine state departments of transportation, the University of Maine, and the U.S. Army Corps of Engineers’ Engineer Research and Development Center’s Cold Regions Research and Engineering Laboratory was organized to assess the potential benefits of geogrid base course reinforcement in flexible pavements more representative of state highways than most previous work—that is, stiffer subgrades and more representative base and asphalt layer thickness.

Purpose and scope of the research project

The purpose of this pooled-fund study was to provide missing data required to help determine whether geosynthetic reinforcement is beneficial at conditions typically experienced in state highways. Pavement layer stresses and strains were measured as a function of traffic loading in order to conform with requirements for modifications to the NCHRP 1-37A, Guide for Mechanistic-Empirical Design of New and Rehabilitated Pavement Structures (<http://www.trb.org/mepdg/>).

The overall objectives of TPF-5(010) were:

1. To determine whether and under what conditions geosynthetics (geogrids and geotextiles) increase the structural capacity of pavements typically constructed by state DOTs, when they are used to reinforce the base layer.
2. To determine whether and under what conditions geosynthetics increase the service life of pavements typically constructed by state DOTs.
3. To measure in-situ stress and strain response of the pavement sections for use in current or future pavement design processes.

The original research proposal, for a total of over \$2.3 million, called for four phases of research on full-scale test sections constructed for research to be trafficked to failure with a heavy vehicle simulator (HVS). The phases were:

1. Geogrid used in test sections with constant subgrade moisture content.

2. Geogrid used in test sections with varied subgrade moisture content caused by freezing and thawing.
3. Geotextile used in test sections with constant subgrade moisture content.
4. Effect of subgrade strength on sections reinforced with geogrid and geotextile.

Funding acquired to date is for the first phase only, and construction of the test sections for this phase is the subject of this report. The Phase 1 research proposal called for testing of reinforced test sections on a relatively soft subgrade (resilient modulus of 34.5 MPa, or 5 ksi) with constant moisture content.

This Phase 1 effort also included the development of a three-dimensional finite element model that simulates the response of flexible pavements to traffic loading. The model includes geogrid reinforcement, and the results generated in the large-scale testing by the loading with the heavy vehicle simulator were used to help calibrate the finite element model (Clapp, 2007).

Experimental design

To simulate traffic conditions of a typical highway, the experimental design was based on a pavement design life of 3×10^6 equivalent single axle loads (ESALs). Based on the 1993 AASHTO design guide for a subgrade of resilient modulus of 34.5 MPa (5 ksi), 610 mm (24 in) of base, 152 mm (6 in) of asphalt is required. The experimental design for this project included two asphalt concrete and two base course thicknesses (Table 1). There were eight test sections, making a 2^3 factorial design--allowing for systematic comparison of the influences of base thickness, asphalt thickness and geogrid presence. Hence, both asphalt and base course savings by utilizing geogrid reinforcement were considered.

Table 1: Test sections for geogrid reinforced pavement.

Constructed Test Section Number	Asphalt Thickness (mm/ in)	Base Thickness (mm/ in)	Geogrid between base and subgrade
1	152/ 6	305/ 12	no
2	102/ 4	305/ 12	no
3	152/ 6	305/ 12	yes
4	102/ 4	305/ 12	yes
5	152/ 6	610/ 24	no
6	102/ 4	610/ 24	no
7	152/ 6	610/ 24	yes
8	102/ 4	610/ 24	yes

Overview of heavy vehicle simulator and traffic application

The machine used to provide traffic loading, the Mark IV heavy vehicle simulator (HVS) was manufactured by Dynatest, Inc. The HVS is 23 m (75 ft) long, 3.7 m (12 ft) wide and 4.1 m (13.5 ft) high and weighs approximately 50,000 kg (110,000 lb). The load on a dual tire assembly can range from 20 to 102 kN (4.5 to 45 kips). Traffic can be uni-directional or bi-directional, and the wheel speed is a maximum 13 km·hr⁻¹ (8 mph). Traffic wander can be uniform or variable. The HVS can simulate several different types of heavy loads.

Dual truck tires were utilized in this project, with each traffic load beginning with a 48.9 kN (11 kip) wheel load (representing a 97.8 kN, or 22 kip, axle load--the maximum that is allowed by several states). The operating pressure of the wheel is 689.5 kPa (100 psi). Traffic was applied in one direction at 12.9 km·hr⁻¹ (8 mph), and allowed to wander over the 0.92-m-width in the test window of each test section. The test window is the central portion of each test section to which the wheel load is applied.

At several times during the trafficking of each test section, trafficking is temporarily suspended and the wheel load applied directly over stacks of sensors that indicate vertical deformation while distance between sensors is recorded. In this way, the total deformation occurring in each section of pavement (asphalt, base and subgrade) can be determined. These tests are referred to as static tests.

Overview of test section construction

The test sections were constructed in the Frost Effects Research Facility (FERF) of the U.S. Army Corps of Engineers' Engineer Research and Developments Center's Cold Regions Research and Engineering Laboratory (ERDC-CRREL) in Hanover, New Hampshire. The FERF is equipped for control of moisture and temperature conditions during construction and traffic testing. The temperature inside the FERF building was kept at approximately 23°C (73°F) during construction.

The structure of the test sections included an asphalt concrete layer over a crushed stone base course over a subgrade soil, AASHTO A-4 (USCS type ML). The concrete floor was 2.44 m (8 ft) below the pavement surface. The bottom layers of the subgrade were already present in the test basin, and the top portion of the subgrade was placed and compacted beginning at a depth of 1.52 m (5 ft) down from the asphalt surface. The geogrid used in these experiments is located at the interface between the subgrade and the base course. The test sections were instrumented with sensors to measure stress, strain, moisture and temperature at strategic locations within the pavements.

Final, constructed subgrade modulus values, measured by a falling weight deflectometer (FWD), of approximately 55.2 to 75.8 MPa (8 to 11 ksi), were achieved by constructing the subgrade of the test sections at near optimum moisture content and maximum dry density and subsequently adding water to the test basin near the top of the subgrade, which resulted in a lowering of the modulus. The 'softening' process took about 5 months. During this time water was added in increments, and periodic monitoring with FWD tests was performed in coordination with moisture content readings.

Purpose and scope of this report

This report documents, in detail, the construction and instrumentation of the test sections. It is being published as a special report for availability on the internet and

through the U.S. Army Engineer Research and Development Center's libraries. Hence, for subsequent publication of performance data, the construction details are available to aid in data interpretation and analyses.

DESCRIPTION OF THE TEST SECTIONS

The test sections were constructed in a test basin that is 6.4-m (21-ft) wide with concrete walls and a floor at 2.44 m (8 ft) from the pavement surface (Fig. 1). Figures 2 a and b show cross-sections of the test basin for test sections 3 & 4 and 7 & 8, respectively. The thickness of the base course is 0.30 m (1 ft) for Test Sections 1 through 4, and 0.61 m (2 ft) for test sections 5 through 8. The asphalt thickness for the east lane (Test Sections 2, 4, 6, and 8) was 102 mm (4 in). The asphalt thickness for the west lane (Test Sections 1, 3, 5, and 7) was 152 mm (6 in).

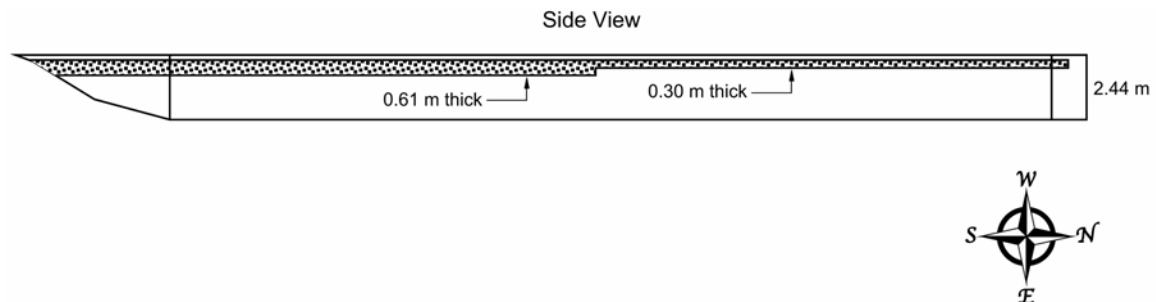


Figure 1.a. Longitudinal, cross section view of test basin showing the two base course thickness.

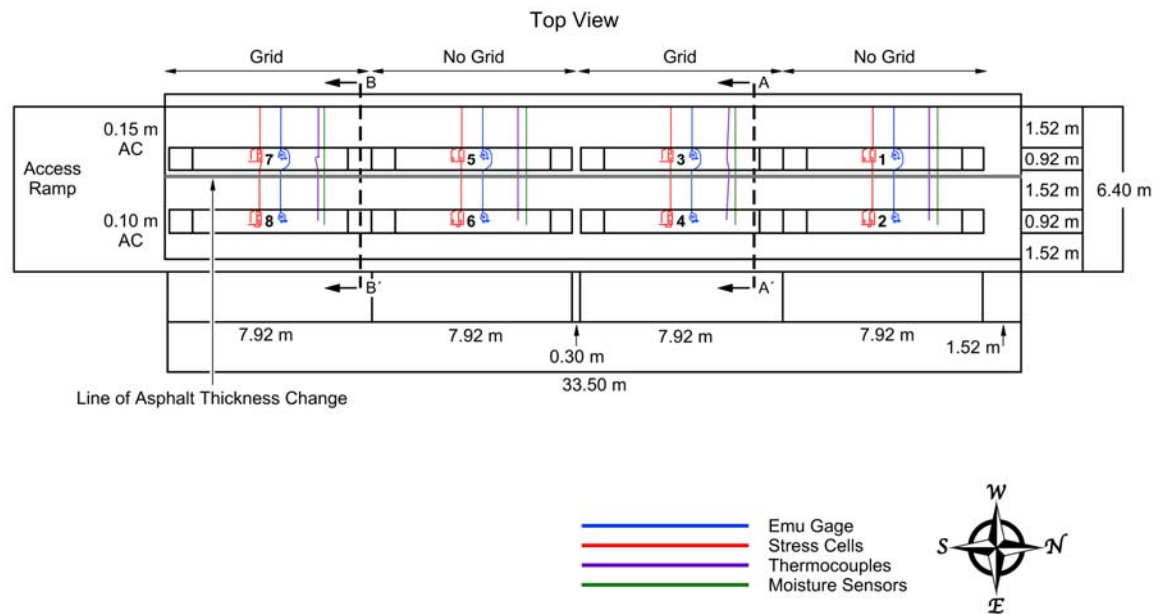


Figure 1.b. Plan view of test basin, indicating test windows (i.e., the long, numbered rectangles, where traffic was applied) and instrumentation.

The subgrade thickness was either approximately 1.5 m (5 ft) or 1.8 m (6 ft). For the previous research project, the test basin was lined with an impermeable membrane to prevent drainage, and a 254-mm (10-in) layer of gravel was placed in the bottom of the test basin (below the subgrade) to facilitate moisture control. The layer of gravel (drainage layer) is separated from the overlying subgrade by a needle-punched geotextile. The bottom gravel layer was used to promote the uniform distribution of water below the subgrade layer for purposes of moistening the subgrade. For this project, the geomembrane liner was removed from the side walls to a depth of 1.5 m (5 ft) from the asphalt surface, and was left in place below that depth.

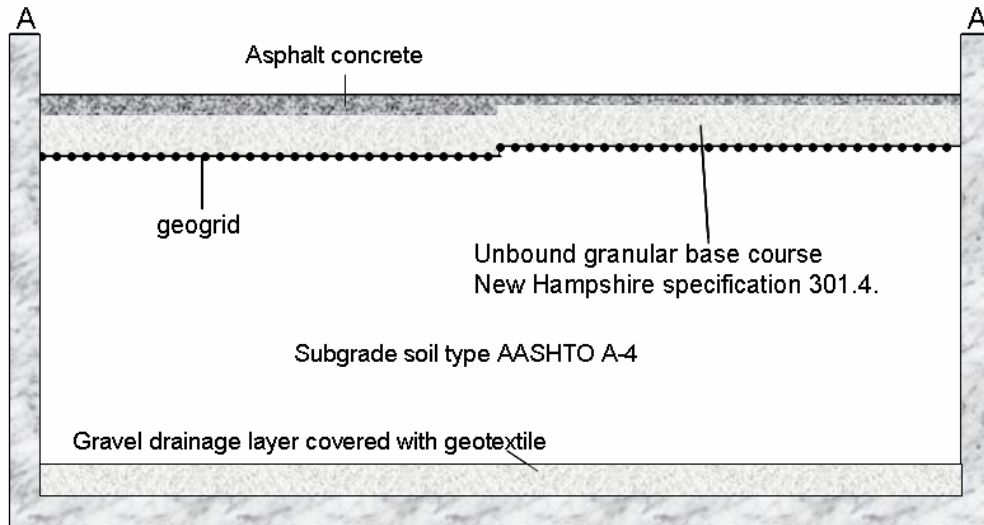


Figure 2.a. Cross sectional view of Test sections 3 and 4, corresponding to A-A', on Figure 1b (not to scale).

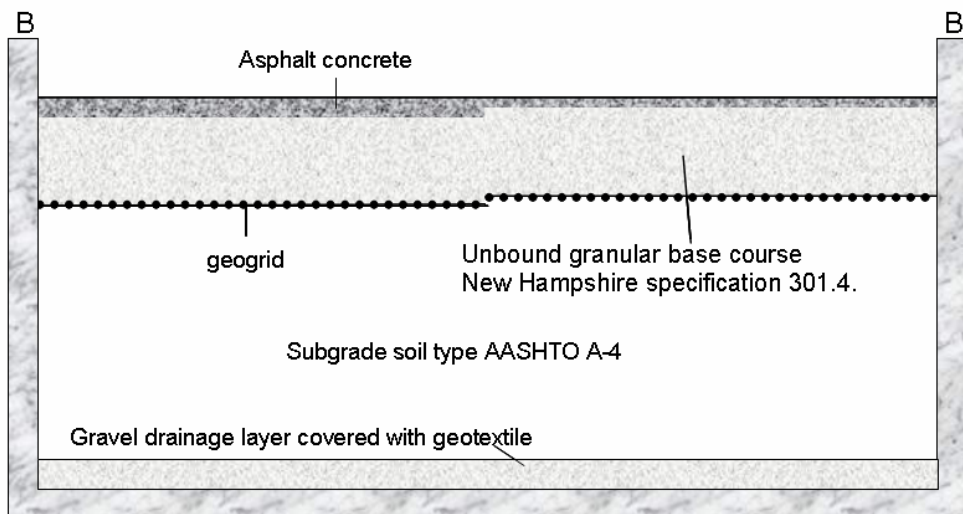


Figure 2.b. Cross sectional view of Test sections 7 and 8, corresponding to B-B' shown on Fig. 1b (not to scale).

The test window, or the portion of the test section to which the wheel load was applied on the surface, is 0.91 m (3 ft) wide by 7.9 m (26 ft) long, with 0.91 m (3 ft)

transition zones on each end (Figs. 1 and 3). The transition zones are where the wheel load was applied and accelerated (on the North side) and decelerated and removed (on the South side), so that the central 6.0 m (20 ft) of the test window were trafficked at constant load and speed. The coordinate system utilized to document the location of sensors within the test windows that is used in Appendix A (as well as marked on each test section) has the origin $(0,0,0)$ located at the surface of the asphalt and at the center of the test window of each test section as shown in Figure 4.



Figure 3. Paved test sections showing test windows (outlined in yellow) to which traffic was applied, including the short transition sections. Traffic was applied in a direction away from the viewer of this image.

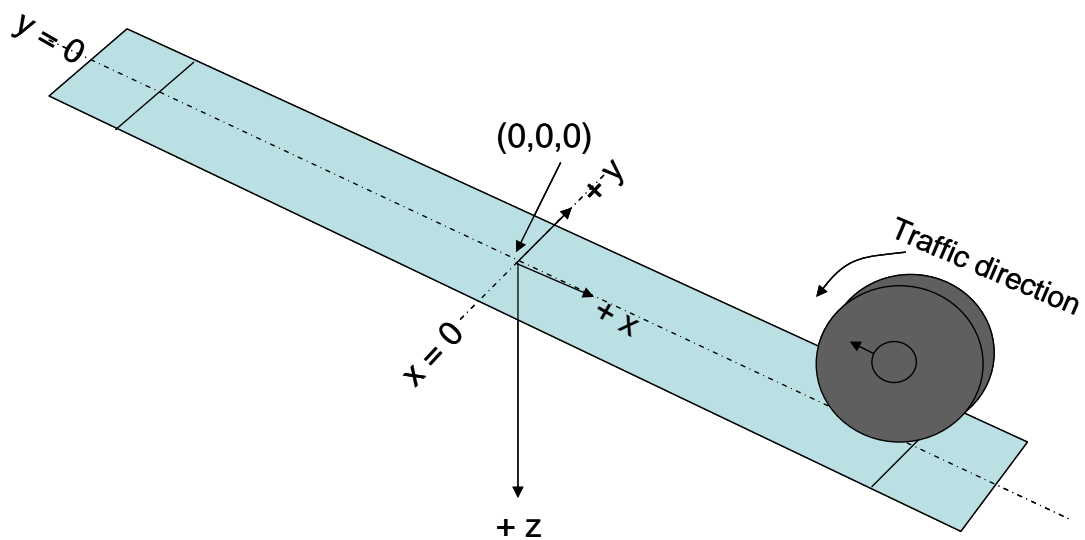


Figure 4. Local coordinate system for each test window. Traffic direction was from North to South.

MATERIAL PROPERTIES

The subgrade, 'Hanover Silt,' is native to the Connecticut River Valley in the local Hanover, NH, area. The base was made of unbound crushed stone obtained from a quarry in Lebanon, NH. The source rock is an amphibolite. It is classified as AASHTO A-1 (USCS type GP-GM--mix of poorly graded gravel and silty gravel). The fines are non-plastic. The base meets New Hampshire specification 301.4 for base course materials. The test soils' grain size distributions, soil classification information, and compaction curves (Modified Proctor) are presented in Tables 2a and b and Figures 5 through 7. Figure 6 also shows California Bearing Ratio determinations for the subgrade soil as a function of soil moisture.

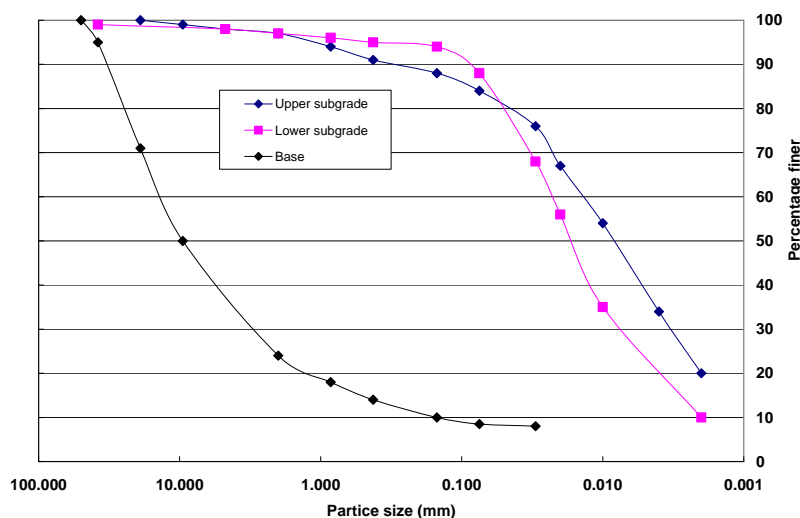


Table 2b. Base soil properties. Dry density and optimum moisture content were determined according to AASHTO T-180 (Modified Proctor).

AASHTO	A-1
USCS	GP-GM
Spec. Gravity	2.7
LL (%)	Not applicable, fines non-plastic
PI	
Optimum moisture content (%)	5
Maximum dry density (kg/m ³ /pcf)	2383/ 149
% passing $\frac{3}{4}$ "	82
% passing #200	5.4

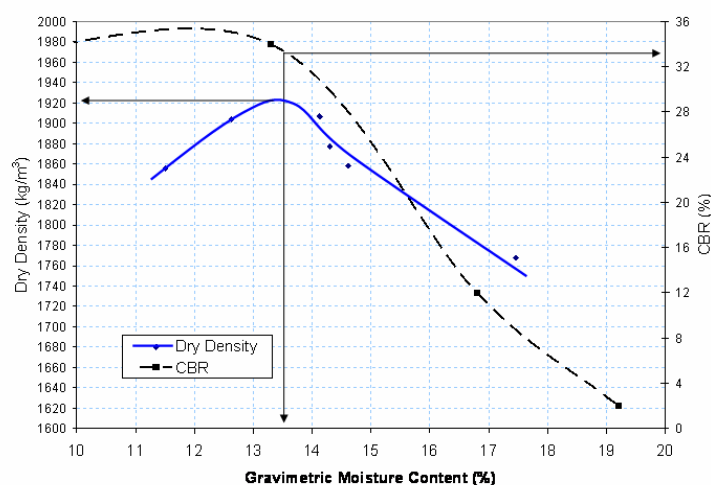


Figure 6. Modified Proctor and laboratory CBR test results for the subgrade soil.

Laboratory determinations of resilient modulus were made for the subgrade and base using AASHTO Standard T-307-99 ‘Determining the Resilient Modulus of Soil and Aggregate Materials.’ Due to the low plasticity of both soils, in-situ sampling was not practical. The resilient modulus subgrade specimens were compacted by hand at optimum water content to the maximum dry density in six lifts--each layer was scarified on the top to promote uniform structure. Specimens were 152 mm (6 in) high by 71 mm (2.8 in) in diameter. The base specimen was 305 mm (12 in) high by 152 mm (6 in) in diameter, and was compacted by pouring the aggregate into the mold and tapping it to promote densification. Neither specimen preparation procedure is specified in AASHTO Standard T-307-99; however, they did produce the densities required to simulate the soil compaction.

The stress conditions used in the tests represent the range of stress states that occur in pavements due to traffic loading. The results of the subgrade and base resilient modulus determinations are summarized in Tables 3 and 4.

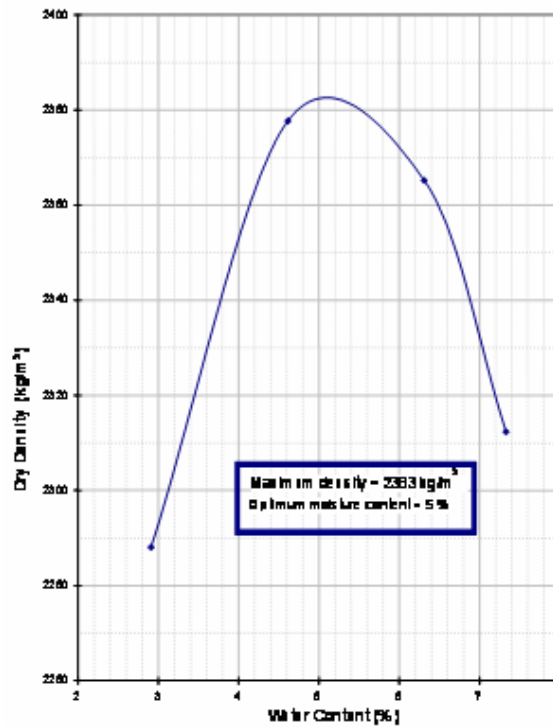


Figure 7. Base course modified Proctor test results.

The laboratory-measured resilient modulus values for saturated subgrade were approximately 30-60% of the values of the subgrade compacted at optimum water content. Further, they were the desired test values for trafficking. Hence, the stiffness of the constructed subgrade was lowered by adding water as described in a subsequent section of the report entitled ‘Test Section Construction.’

Table 3. Resilient Modulus values for four compacted subgrade specimens—three compacted at maximum dry density and optimum moisture content, one compacted at maximum dry density then subsequently saturated prior to testing.

Specimen	Water content (%) (gravimetric)	Dry density (Mg m ⁻³ / lb ft ⁻³)	Confining Pressure (kPa)	Peak Cyclic Stress (kPa)	Resilient Modulus (MPa)	Resilient Modulus (psi)
15-4	13.1	1.827/ 114.0	13.8	24.6	77	11,170
			13.8	37.3	72	10,440
			13.8	49.1	71	10,300
			13.8	61.6	73	10,590
			27.6	24.5	93	13,490
			27.6	36.9	88	12,760
			27.6	49.6	83	12,040
			27.6	61.4	82	11,890
			41.4	25.1	116	16,820
			41.4	49.5	97	14,070
			41.4	61.6	93	13,490
15-3	13.1	1.840 / 114.4	13.8	24.5	110	15,950
			13.8	37	86	12,470
			13.8	49.1	81	11,750
			13.8	61.6	81	11,750
			27.6	24.5	124	17,990
			27.6	36.5	105	15,230
			27.6	49	102	14,790
			27.6	61.7	94	13,630
			41.4	24.9	139	20,160
			41.4	36.9	117	16,970
			41.4	49.1	115	16,680
			41.4	61.9	110	15,950
15-2	13	1.840 / 114.4	13.8	24.4	138	20,020
			13.8	37.4	91	13,200
			13.8	49.5	84	12,180
			13.8	61.7	87	12,620
			27.6	24.5	103	14,940
			27.6	37.7	83	12,040
			27.6	49.6	85	12,330
			27.6	61.5	82	11,890
			41.4	37	97	14,070
			41.4	49.7	92	13,340
			41.4	62	90	13,050

Table 3, continued. Resilient Modulus values for four compacted subgrade specimens—three at maximum dry density and optimum moisture content, one at maximum dry density then subsequently saturated.

Specimen	Water content (%) (gravimetric)	Dry density (Mg m ⁻³ / lb ft ⁻³)	Confining pressure (kPa)	Peak cyclic stress (kPa)	Resilient modulus (MPa)	Resilient modulus (psi)
GeoSat-1 (saturated)	Initial – 13.0 Final – 21.6	(1.74 /108.7)	13.8	27.6	25	3,650
			13.8	41.2	25	3,630
			13.8	55.5	30	4,420
			13.8	68.7	33	4,760
			27.6	28.1	31	4,510
			27.6	41.3	31	4,470
			27.6	54.8	32	4,570
			27.6	68.7	33	4,840
			41.4	28.0	32	4,680
			41.4	41.9	47	6,830
			41.4	55.7	42	6,150
			41.4	69.7	38	5,550

Table 4. Resilient Modulus values for a base layer specimen compacted at optimum water content to maximum dry density.

Water content (%) gravimetric	Dry density (Mg m ⁻³ / lb ft ⁻³)	Confining pressure (kPa)	Peak cyclic stress (kPa)	Resilient modulus (MPa)	Resilient modulus (psi)
2.9	2.258/ 141.0	34.5	30.8	155	22,481
		34.5	60.8	224	32,488
		34.5	92.1	237	34,373
		69.0	62.2	265	38,435
		69.0	123.0	291	42,205
		69.0	186.0	334	48,442
		103.5	59.5	348	50,473
		103.5	91.5	352	51,053
		103.5	185.8	415	60,190
		137.9	92.1	396	57,434
		137.9	123.9	504	73,099
		137.9	245.2	451	65,412

The geogrid used in these experiments, Tensar BX1200, was chosen because it has been used in similar studies in the past, and it is relatively easy to instrument with strain gages (Fig. 8). This allows comparison between test results generated by this study and others reported in the literature. The selection of this particular geogrid does not imply endorsement of it. The mechanical properties as provided by the manufacturer for the geogrid are listed in Table 5. Additional information can be found at the following link: http://www.tensarcorp.com/uploadedFiles/SPECTRA_MPDS_BX_8.05.pdf

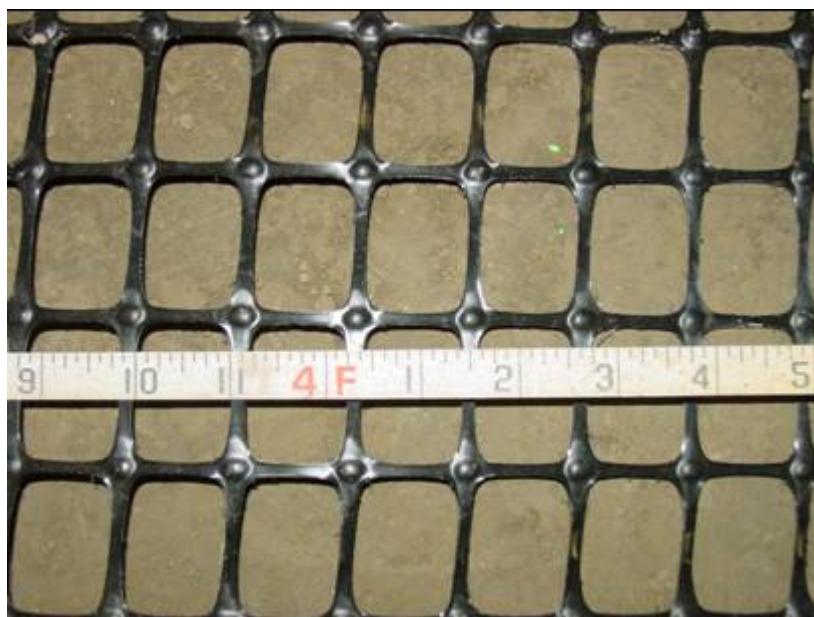


Figure 8. Tensar® BX1200 geogrid.

Table 5. Properties of geogrid used in the test sections.

Aperture size mm (in)		Wide-width tensile strength at 2% strain*, kN m^{-1} (lb ft^{-1})	
Machine Direction	Cross-machine direction	Machine Direction	Cross-machine direction
25 (1.0)	33 (1.3)	6.0 (410)	9.0 (620)

*Determined according to ASTM D6637.

The hot mixed asphalt (HMA) material conformed to the New Hampshire specifications for a type B base course and Type F surface course. Type B gradation requires 95-100% of the aggregates pass the 19-mm (3/4-in) sieve. The Type F requires 95-100% passing the 9.5 mm (3/8-in) sieve size. The gradations and range of asphalt content for both mixes are presented in Table 6, and measured gradations provided by the Maine DOT based on tests of an asphalt core are provided in Table 7. Tests on the asphalt cores also indicated that the asphalt aggregate had a bulk specific gravity of 2.6 and an average air voids content of 2.1%.

The asphalt binder grade was PG 64-28. This is a commonly used asphalt grade used for highway construction by paving contractors in the Hanover, New Hampshire area.

Table 6. NHDOT asphalt concrete gradation and asphalt content ranges.

<i>Sieve size</i>	<i>Type B – Base Course, percentage passing</i>			<i>Type F – Surface Course, percentage passing</i>		
	<i>Min</i>	<i>Desired</i>	<i>Max</i>	<i>Min</i>	<i>Desired</i>	<i>Max</i>
31.8 mm (1-1/4in)						
25.4 mm (1in)						
19.1 mm (3/4in)	95	100	100			
12.2 mm (1/2in)	70	81	92			
9.5 mm (3/8in)	60	71	80	95	100	100
4.75 mm (No. 4)	42	50	57	64	71	80
2.00 mm (No. 10)	28	32	38	44	50	55
0.85 mm (No. 20)	16	20	24	25	30	35
0.425 mm (No. 40)	9	13	17	15	20	25
0.180 mm (No. 80)	3	7	11	6	11	16
0.075 mm (No. 200)	0	3	4	2	4	6
% Asphalt Content*	4.8	5.25	6.0	6.25	6.5	7.0

*The asphalt content is based on the use of aggregates with a specific gravity of 2.65 to 2.70.

**Table 7. Asphalt concrete gradation measured on asphalt cores taken after paving.
(There was no distinction between base and surface course.)**

<i>Sieve size</i>	<i>Percentage passing</i>
31.8 mm (1-1/4in)	
25.4 mm (1in)	100
19.1 mm (3/4in)	98
12.2 mm (1/2in)	92
9.5 mm (3/8in)	85
4.75 mm (No. 4)	57
2.36 mm (No. 8)	43
0.60 mm (No. 30)	23
0.35 mm (No. 50)	14
0.152 mm (No. 100)	8
0.075 mm (No. 200)	5
% Asphalt Content	5.8

INSTRUMENTATION

Each test section was instrumented with moisture and temperature sensors, triaxial strain gages (ϵ mu coils) and pressure cells. Figures 9 a and b are a typical plan view and cross-section of the portion of a geogrid test section in which instrumentation was installed, respectively. The locations of each sensor are documented in detail in Appendix A. In addition to the installed coils, a hand-held ϵ mu coil was placed over the asphalt surface to measure the vertical deformation in the asphalt layer only when deformation readings were made. Additional details about each sensor are provided below.

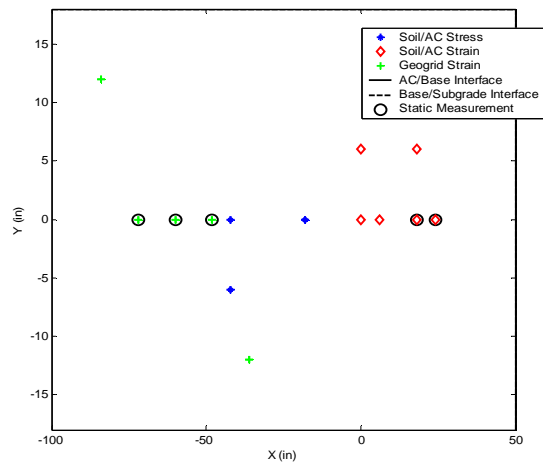


Figure 9a. Plan view of instrumentation of a geogrid test section. Locations of static load tests are also shown.

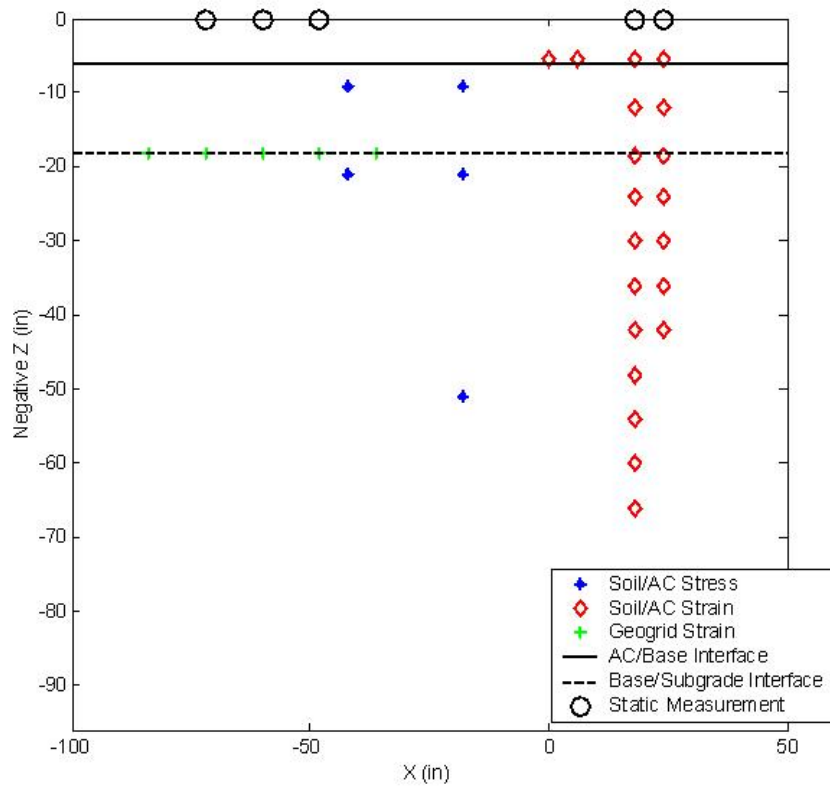


Figure 9b. Cross-sectional view of instrumentation of a geogrid test section. Locations of static load tests are also shown.

Temperature Sensors

Copper-constantan, Type T, thermocouples were installed to measure temperatures in the asphalt and soil layers--the accuracy of these thermocouple measurements is $\pm 0.5^{\circ}\text{C}$. (The Type T thermocouples are measured differentially at a range of ± 2.5 mV which yields a resolution of 0.33 μV .) Temperatures were recorded by Campbell Scientific CR10X data loggers (described below), which have internal thermistors that provide a reference temperature. The data logger was programmed to record temperature and moisture measurements every 4 hours.

Moisture Sensors

ECH₂O™ soil moisture sensors (Echo probes), model EC-20 (200-mm-long) were installed to record volumetric soil moisture content in the base course and subgrade (Fig. 10). Echo probes measure the dielectric constant of the surrounding soil by finding the rate of change of voltage on a sensor embedded in the soil. The relative permittivity (i.e., dielectric constant) of water is approximately 80, that of most rock-forming minerals is around 4, and air is 1. This high value for water results in relatively large changes in the permittivity of soil when the water content changes. EC-20 probes' typical accuracy in medium-textured soil types is $\pm 4\%$, and the resolution is 0.1%. (The ECHO soil moisture probes are measured differentially at the ± 2500 mV range. At that range the resolution of the measurement is 333 μV .)



Figure 10. Soil moisture sensor image.

Pressure cells to measure stress

Geokon® soil pressure cells were installed in the base course and subgrade of each test section for the purpose of measuring soil stress (Fig. 11). The pressure cells consist of two circular stainless steel plates welded together around the periphery enclosing a fluid connected to a pressure transducer through a high pressure stainless steel tube. The pressure transducer outputs a voltage that is calibrated to produce a stress measurement.

The pressure cells were installed in three perpendicular directions--vertical, longitudinal (in the direction of traffic) and transverse (perpendicular to the direction of traffic). The pressure cells in the transverse direction were offset 152 mm (6 in) in order to avoid measurement directly beneath the wheel load, in which case the transverse component of stress may be negligible.

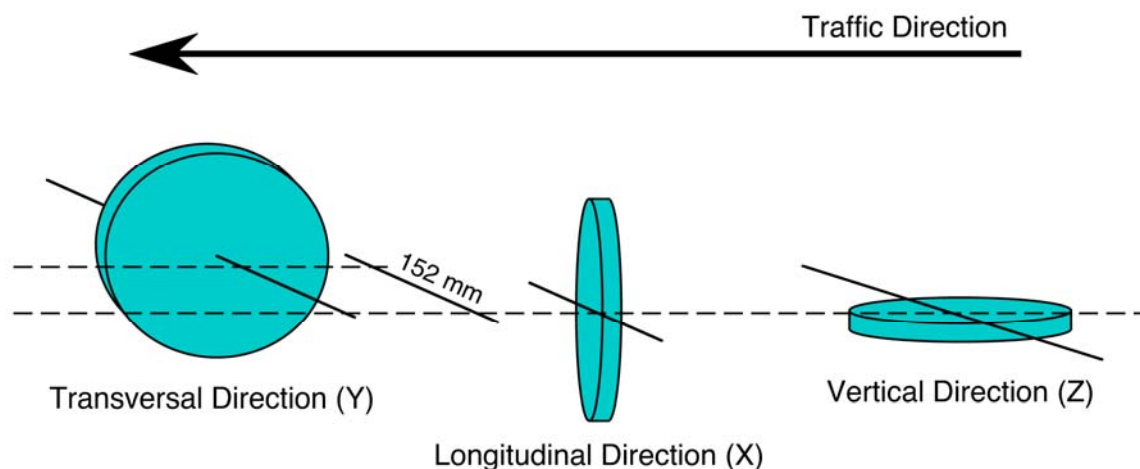


Figure 11. Diagram showing orientation of pressure cells.

Soil and Asphalt Strain Sensors

Electromagnetic induction ($\epsilon\mu$, or $\epsilon\mu$) coils were installed to measure deformations in the vertical and horizontal directions. They can be used for static or dynamic deformation measurement—in this project, they were used for determination of permanent deformation via static measurement. They were manufactured and calibrated at ERDC-CRREL. The $\epsilon\mu$ coils do not touch each other, but ‘float’ in the soil, similar to small stones embedded in a fine soil mass.

These coils work in pairs—one coil, called the sender, is energized by an external power supply. A companion coil, the receiver, is located within the electromagnetic field of the sender, and produces an induced current that is proportional to the distance between the coils. When a traffic load compresses a pavement layer, the change in inter-coil distance is detected by a change in induced voltage that increases as the distance between coils decreases. Based on the known initial distances between coil pairs, the average strain for a layer can be calculated. The $\epsilon\mu$ coils and measurement system used in this project is the same as used in a previous project; and is described in detail in Janoo, et al. (2003), including detailed calibration information. This report can be downloaded from

<http://www.crrel.usace.army.mil/library/technicalreports/TR03-5.pdf>.

Special calibration jigs were made to determine voltage output as a function of sensor spacing. For both coplanar and coaxial calibration, the transmitting coil was fixed and the receiving coil was on a moveable frame, initially at 140 mm away from the transmitting coil. After excitation, voltage measurements were made as the distances between the coils were increased in increments up to 25.4 mm. The following equation gave a good fit to the data:

$$V = aD^n$$

where D = the static distance between the transmitting and receiving devices, V = the demodulated (d.c.) ‘static’ voltage from the coils and a and n are the regression coefficients for a pair of coils.

Geogrid Strain Gages

Ten electrical resistance strain gages were fastened to the geogrid in each test section in order to make longitudinal and transverse strain measurements on the top and bottom of the grid. Five strain gages were fastened on the upper side of the geogrid and five were fastened at corresponding locations on the lower side of the geogrid. The strain gages used were Texas Measurements model FLA-5-23. They are capable of measuring up to 3% strain, and have a gage factor of 2.16. The gages had a copper-nickel alloy foil element, 0.003- to 0.007-mm (0.00012 to 0.00027 in) thick on a 10 mm x 3 mm (0.39 in x 0.12 in) epoxy backing, which was attached to the geogrid ribs using two-part epoxy. Each gage had pre-soldered lead wires that were connected into the ERDC-CRREL data acquisition system. Readings were taken by applying an excitation voltage of approximately 2500 mV.

Measurements utilized a Wheatstone Bridge (Fig. 12).

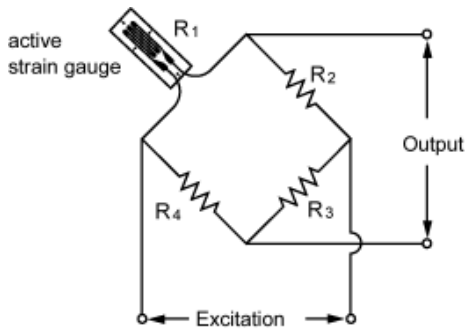


Figure 12. Wheatstone bridge configuration used for strain gage measurement (http://www.straingage.com/strain_gage/what_strain.php, accessed on 5 December 2007).

Using a Wheatstone Bridge with a constant excitation voltage, changes in gage resistance are directly proportional to changes in strain of the gage. The Wheatstone Bridge circuit converts the resistance change into voltage output via the following equation:

$$e = \frac{R_1 R_3 - R_2 R_4}{(R_1 + R_2)(R_3 + R_4)} E,$$

Where e is the voltage output of the strain gage, E is the excitation voltage, the R values are as defined in Figure 12. Assuming that all of the resistances (R_1 to R_4) are equal and that the change in resistance of the gage (ΔR_1) is much smaller than its unstrained resistance, this equation simplifies to:

$$\Delta e = \frac{\Delta R}{4R} E = \frac{E}{4} K \varepsilon \text{ where } K \text{ is the gage factor and } \varepsilon \text{ is the strain experienced by the gage.}$$

More information about the theory of operation can be obtained at: www.straingage.com/strain_gage/what_strain.php. Initial resistance readings on the strain gages verified that the strain gages were operational.

The strain gages were applied to the geogrid in the same manner as described in Helmstrom, et al. (2006). The surface of the individual ribs of the geogrid, on which the strain gages were attached, were first roughened with emery cloth and then coated with Texas Measurements poly-primer. A piece of Scotch tape was applied to the gage backing and Cyanoacrylate CN adhesive was applied to the gages. The gages were then centered on the prepared ribs and the tape held them in place while the adhesive cured. Direct pressure was applied to the gage for a minimum of one minute, and the tape was not peeled from the back of the gage until a minimum of five minutes curing time.

Data acquisition system

All cables of the sensors embedded in the test sections were routed underground through test section ‘portholes’ to an instrumentation tunnel located on the west side of the test sections. The cables were connected to boards on which they were properly organized and then routed to the appropriate data acquisition system (Fig. 13).

The data acquisition for this project consisted of four subsystems. The moisture and temperature sensors were connected to a system of commercially available, Campbell Scientific, CR10X data loggers. The data loggers were networked with a computer located in the control room of the FERF facility, which was then accessed via an internal network by researchers. The CR10X is a fully programmable datalogger / controller with non-volatile memory and battery-backed clock. It is a small, rugged, sealed module. The CR10X has an input voltage range of +/- 2500 mV to +/-2.5 mV. To handle the large number of sensors three Campbell Scientific AM416 multiplexers were used. The AM416 is a multi-channel relay board with gold clad silver alloy screw-down terminal contacts. The initial contact resistance is less than 0.1 ohms and the switching time between relays is less than 1 ms.

A second subsystem consisted of the sensors and controls within the heavy vehicle simulator. This system is an integral part of the HVS, and keeps records of the number of traffic passes, traffic wander, and the average load intensity for each pass. The third data acquisition subsystem was the laser profilometer that is connected to a notebook computer that automatically logs data related to rut depth measurement whenever the profilometer is operating. The laser profilometer is commercially available from Dynatest and was developed for the purpose of accurately measuring ruts developed by HVS traffic.

The fourth subsystem is a high-speed data acquisition system developed at the ERDC-CRREL to collect and preprocess the signals from the stress and strain sensors. National Instruments LabVIEW was used in conjunction with a NI 6033E data acquisition card to read the outputs of the emu coils and the strain gages. The NI 6033E has 64 single-ended analog input channels. The resolution is 16 bits, or 1 in 65,536. The max sampling rate is $100\text{kS}\cdot\text{s}^{-1}$. The accuracy at full scale is 1.15 mV. For data security and reliability purposes, this computer was networked with only one other computer that, in turn, was connected to a larger internal network. The hardware and software of this data acquisition subsystem were developed by CRREL electronic engineers because no suitable commercially-available system was found at the time of its development.

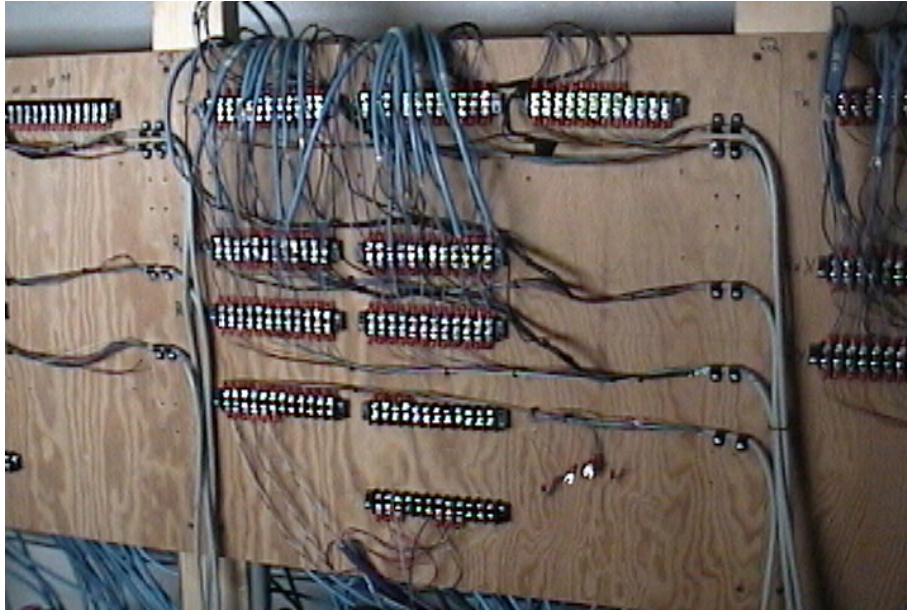


Figure 13. Cable connections on boards located in the instrumentation tunnel.

CONSTRUCTION OF THE TEST SECTIONS

Subgrade construction

The subgrade was placed in layers approximately 152-mm (6-in) thick on top of soil that was already in-place to a depth of 1.52 m (5 ft) below the paved surface. The subgrade soil was placed in the test basin by a front-end loader, and a bull dozer tractor spread the soil to a grade slightly higher than the target for a given layer (Fig. 14). The soil was then cultivated with a roto-tiller to promote uniform moisture distribution and the moisture content of the soil was measured with a nuclear gage (Fig. 15). The moisture deficit was established, and the amount of water needed to reach the moisture target was calculated. The required amount of water was then added in strips of 1.52 m (5 ft) across the width of the test section. The soil was cultivated again and then compacted. A smooth steel roller and was used for compaction until the target density was achieved—a plate compactor was used to compact the soil near the edges of the test basin (Fig. 16). Typically, eight passes with the roller were required to achieve compaction. Once compaction was achieved, sensors were installed, and a new soil lift was placed and the process was repeated again until the subgrade was completed at the planned grade.



Figure 14. Front end loader and bull dozer tractor that were used to build the test sections.



Figure 15. Cultivating the soil to facilitate moisture absorption and uniform distribution.



Figure 16. Plate compactor used to compact the edges of the test section.

Quality control

Moisture and density measurements were made on each layer to ensure that it was constructed near optimum moisture content and maximum dry density. Measurements were made with a Troxler® 3450 nuclear density meter in the direct mode with the probe inserted 152 mm (6 in) into the soil. Direct transmission readings were taken for one minute duration, which yield a precision of $2.6 \text{ kg}\cdot\text{m}^{-3}$ ($0.15 \text{ lb}\cdot\text{ft}^{-3}$) and composition error of $8.0 \text{ kg}\cdot\text{m}^{-3}$ ($0.50 \text{ lb}\cdot\text{ft}^{-3}$) for dry density and precision of moisture at $240 \text{ kg}\cdot\text{m}^{-3}$ ($15 \text{ lb}\cdot\text{ft}^{-3}$) of $5.5 \text{ kg}\cdot\text{m}^{-3}$ ($0.87 \text{ lb}\cdot\text{ft}^{-3}$). Appendix B contains the moisture and density measurements for each layer constructed. The average as-built subgrade moisture content was 12.2 percent compared to the modified Proctor optimum moisture content of 13.3 percent. The average subgrade density was $1858 \text{ kg}\cdot\text{m}^{-3}$ ($116.0 \text{ lb}\cdot\text{ft}^{-3}$) compared to the maximum modified Proctor density of $1922 \text{ kg}\cdot\text{m}^{-3}$ ($120.0 \text{ lb}\cdot\text{ft}^{-3}$). This corresponds to 97 percent compaction.

For each test section, drive-cylinder specimens were obtained and ASTM D 2937, Standard Test Method for density of soil in place by the drive-cylinder method, was used to determine in-situ, dry unit weight at the top of the subgrade at the line bounding the north edge of the traffic/transition window, in the middle of the traffic window and at the line bounding the south edge of the traffic/transition window. The values obtained in this manner are listed in Table 8.

Table 8. Dry density measurements on top of subgrade, determined according to ASTM D 2937.

Test Section	Dry density (kg·m ⁻³ / pcf)		
	North	Middle	South
1	1907/ 119.1	1940/ 121.1	2027/ 126.5
2	1932/ 120.6	1894/ 118.2	2008/ 125.4
3	2044/ 127.6	2028/ 126.6	1912/ 119.4
4	1997/ 124.7	1948/ 121.6	1966/ 122.7
5	1925/ 120.2	1832/ 114.4	1829/ 114.2
6	1840/ 114.9	1852/ 115.6	1955/ 122.0
7	1896/ 118.4	1908/ 119.1	1859/ 116.1
8	1837/ 114.7	1866/ 116.5	1834/ 114.4

Strength measurements made on the subgrade surface

Two types of measurements were made on the top of the finished subgrade and used to obtain estimates of the California Bearing Ratio at several points—dynamic cone penetrometer (DCP) and Clegg Impact Hammer. The CBR estimates based on these readings are contained in Appendix C. The DCP test apparatus used is manufactured by Kessler Soils Engineering Products, Inc. The DCP hammer had a mass of 8 kg (17.6 lb). The DCP–CBR conversions were obtained using an automated Excel spreadsheet provided by the instrument manufacturer, which utilized the following empirical correlation (Webster, et al., 1992):

$$CBR(\%) = \frac{292}{\left(\frac{mm}{blow}\right)^{1.12}}$$

The Clegg impact hammer is essentially an AASHTO compaction hammer fitted with a piezoelectric accelerometer (Fig. 17).



Figure 17. Clegg impact hammer.

Transitions between test sections

In order to construct the test sections so that the final asphalt surface would be level at the same elevation and accommodate the differences in asphalt and base course thickness, adjustments were made to the elevations of the top of the subgrade. This was accomplished by using a barrier constructed of wood to compact soil against when the subgrade soil in the adjacent area of the test basin was finished at a higher elevation. The soil compacted easily and the transitions were quite sharp as shown in Figure 18.



Figure 18. Image showing differences in elevation of the top of the subgrade between test sections.

Installation of instrumentation

Prior to any soil placement marks were made on the four sides of the test basin to indicate the depth (vertical) and horizontal locations of each sensor. As the construction progressed, wires were stretched East-West to matching locations on opposite sides of the test basin in order indicate the location of the center of each sensor (Fig. 19).

When placing a sensor, a small amount of soil was hand-excavated from the compacted lift surface to place the sensor, and a trench was hand-excavated for the cable that connected the sensor to a data logger located on the outside of the test basin (Fig. 20). The cables were placed into the trenches with ample slack. They were routed through the nearest of four ‘port holes’ in the west side of the test basin (e.g., Fig. 19). Great care was taken to restore the soil density after the installation of each sensor and wire.



Figure 19. Image of instrumentation installation, showing wire extended across the test basin for the purpose of precisely locating sensors.



Figure 20. Image (top view) of pressure cells during installation showing trenches and cable.

During installation of the emu coils, the surface of the soil was raked smooth and level, and, if necessary, a small amount of soil was hand-excavated so that when the coils were installed they were level and were placed at their precise 'x, y, z' coordinates. A template was used to keep the distance between emu coils constant and at right angles (Fig. 21). For placement of the emu coils at the bottom of the asphalt layer, fresh asphalt concrete was excavated by hand to install the sensors at the bottom of the asphalt concrete layer (Fig. 22). Then, asphalt concrete was hand-placed on top of them and the

asphalt concrete was compacted as usual. (Asphalt paving is discussed in more detail in a subsequent section.)



Figure 21. Image of installation mold for placement of three ϵ mu coils.



Figure 22. Installing ϵ mu coils in the hot asphalt concrete.

Geogrid installation and placement of base course layer

For the geogrid reinforced test sections, an instrumented geogrid sheet was installed over the finished subgrade so that the center of the geogrid sheet was aligned with the center of the test window (Fig. 23). Small amounts of base course material were

placed over the geogrid sheet at the middle to hold it in place. The sheet was then stretched by hand and anchored by placing additional base material until the sheet was wrinkle-free, aligned and at the intended location (Figs. 24, 25).

The strain gages and their lead wires were covered with sand size material sieved from the base course material. This was done to protect these delicate sensors from potential load concentrations caused by larger aggregate particles. The remaining base course material was placed in 152-mm (6-in) layers, moistened and compacted until the target moisture and density were achieved. Voltage readings of the strain gages attached to the geogrid were not made before and immediately after construction (this was an oversight); however, during testing, initial deformation readings were made immediately prior to trafficking each test section with the HVS.

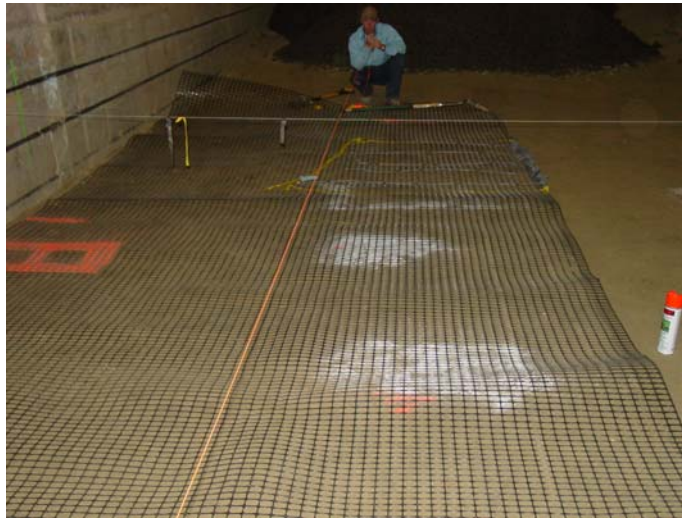


Figure 23. Alignment of instrumented geogrid with tire path—the measuring tape is in the center of the test window.



Figure 24. Geogrid partially covered with base course aggregate.



Figure 25. Close-up of geogrid and base aggregate particles.

The base aggregate was placed in layers approximately 152-mm (6-in) thick. It was moved to the test basin by a front-end loader, and a bull dozer tractor spread it to a grade slightly higher than the target for a given layer. It was rolled with a smooth steel roller to achieve compaction—usually requiring about eight passes. For each layer, the moisture deficit was established, and the amount of water needed to reach optimum moisture content was determined and then added to the aggregate. Although the optimum

moisture content of the base aggregate was 5%, it was not possible to achieve this water content due to the highly permeable nature of the aggregate—the moisture had drained by the time moisture content measurements were made for quality control purposes. Quality control was performed on the base course layer as described above, and the average base course density was $2268 \text{ kg}\cdot\text{m}^{-3}$ ($141.6 \text{ lb}\cdot\text{ft}^{-3}$) compared to the modified Proctor maximum dry density of $2383 \text{ kg}\cdot\text{m}^{-3}$ ($148.8 \text{ lb}\cdot\text{ft}^{-3}$). This corresponds to 95 percent compaction.

Asphalt paving

The test sections were paved with hot mixed asphalt concrete by a local contractor according to New Hampshire Department of Transportation specifications. The process began by hand placement of the asphalt near all the edges of the test basin (Fig. 26). The asphalt was subsequently brought in by dump truck and spread with a paver (Fig. 27). The asphalt was placed in a 50-mm (2-in) base layer, followed by a 50- or 100-mm (2- or 4-in) surface course (e.g., Fig. 27). The asphalt concrete temperature during placing and compacting was monitored to assure that it was placed according to NH specifications—between 135°C and 154°C ($275\text{-}310^{\circ}\text{F}$). Compaction was achieved by using a vibratory paving roller (Fig. 28). Nuclear density measurements were made during rolling to ensure proper compaction and air void content (Fig. 28). Thermocouples and pressure cells were installed embedded in the hot mixed asphalt during paving in the same manner as the emu gages were (as described above) (Fig. 22). Figure 29 shows the paved test sections and marked test windows.



Figure 26. Hand placement of asphalt near north edge of test basin.



Figure 27. Image of paving operation during placement of the surface course of asphalt. The dump truck containing the asphalt concrete is in the background and the paver is shown in the middle.

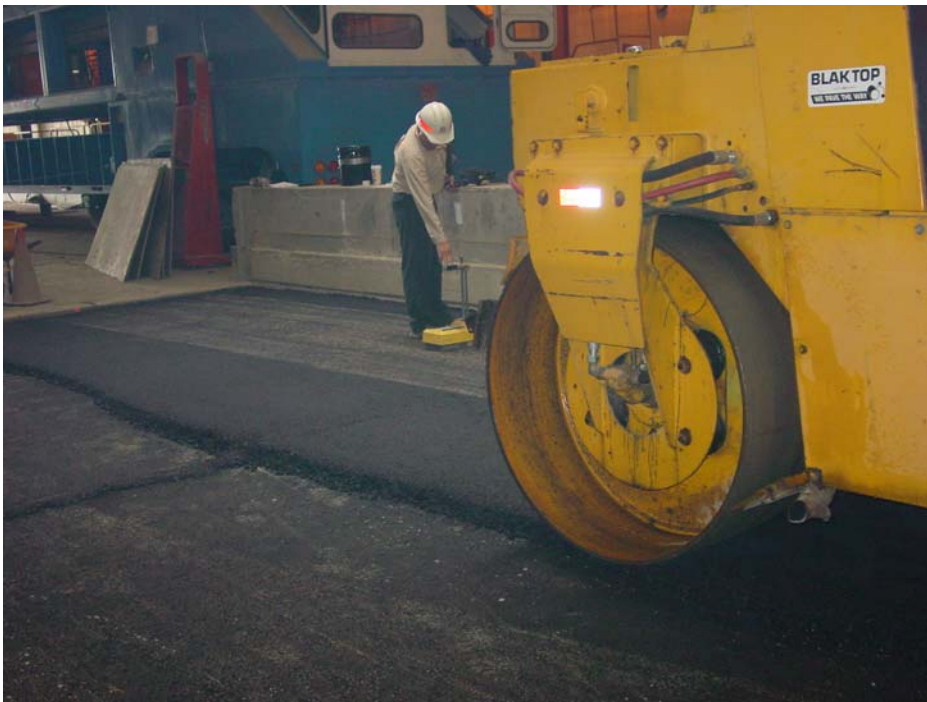


Figure 28. Image of steel drum roller compacting the surface of the asphalt concrete layer. Note nuclear gage in the middle of the image.



Figure 29. Paved test sections and marked test windows. The traffic was applied in the direction away from the viewer, hence the loading transition zone is in the foreground of the image.

Dynamic modulus values of asphalt

Laboratory-determined dynamic modulus values of the asphalt were required for the modeling effort (e.g., Clapp, 2007). Hence, after construction, three 100-mm(4-in) diameter specimens were obtained approximately 0.3 m from the edge of the test basin and shipped to Worcester Polytechnic Institute for determination of dynamic modulus values according to AASHTO TP 62-03. The results are listed in Table 9.

Table 9. Dynamic modulus values of asphalt placed in test basin determined according to AASHTO TP 62-03.

Temp (°C/°F)	Frequency (Hz)	Stress (kPa/ psi)	Dynamic modulus (MPa/ksi)
4.4/ 40	25	30.1/4.37	17160/ 2490
	10	32.0/ 4.64	15200/ 2210
	5	32.4/ 4.70	14250/ 2067
	1	39.2/ 5.69	12770/ 1852
	0.5	37.1/ 5.38	11490/ 1667
	0.1	31.6/ 4.58	8742/ 1268
21.1/ 70	25	Corrupt data	Corrupt data
	10	Corrupt data	Corrupt data
	5	28.1/ 4.08	4481/ 650
	1	37.3/ 5.41	2902/ 421
	0.5	36.1/ 5.24	2318/ 336
	0.1	30.2/ 4.38	1495/ 217
37.8/ 100	25	12.5/ 1.81	3675/ 533
	10	25.9/ 3.76	2670/ 387
	5	29.5/ 4.28	2077/ 301
	1	37.0/ 5.37	1129/ 164
	0.5	36.4/ 5.28	870/ 126
	0.1	30.3/ 4.40	536/ 78

Water addition to decrease subgrade stiffness

After the test sections were constructed, FWD analyses (described below) indicated that the subgrade stiffness ranged from approximately 109-138 MPa (16-20 ksi) (Table 10). Water was then added to the subgrade over an extended period to reduce the stiffness to come as close as possible to the original target modulus of approximately 34.5 MPa (5 ksi). A 150 mm (6 in) width of asphalt was removed from along the sides of the test basin, to expose the base layer of crushed rock, and short sections of PVC tubing were installed in the center of the test basin area to a depth of 50 mm (2 in) into the subgrade in order to assure that water addition never resulted in saturation of the base aggregate layer (Fig. 30).



Figure 30. Image showing trench formed by asphalt removal from the edge of the test basin. Water was added to the base layer exposed in the trench to decrease the stiffness of the subgrade layer.

The amount of water required to saturate the subgrade for a thickness of 6 feet was estimated at 47.47 m^3 (5,400 gallons). Water was added in increments of 0.92 m^3 (105 gallons) at a time, with application intervals being at least 48 hours. Water was added with a garden hose (with an attached water meter) while walking the length of the trenches so that water did not pond at any one location. Water levels were checked in the wells during and immediately after adding the water to assure that the base did not become saturated by this process. The volumetric soil moisture sensors were monitored with time, and FWD tests were performed periodically on the test sections in order to obtain back-calculated estimates of the subgrade resilient moduli values. Figure 31 shows the location of the FWD test points—the numbers on the plan indicate the FWD testing points, and they are located in the transition zone for the wheel load application in the test section of the same number. The watering procedure was continued until there was a leveling of the water content values in the subgrade and the back-calculated resilient modulus values were relatively constant.

Table 10 contains the subgrade and base modulus values in December 2005 and in May 2006, as measured with the FWD, just prior to testing. The modulus values were back-calculated with the commercially-available ELMOD 5 program from Dynatest utilizing the Odemark-Boussinesq method of equivalent thickness in which the outer geophone readings are used to determine the non-linear characteristics of the subgrade and the inner geophones are used to determine the upper pavement layer moduli (Dynatest International). The depth to bedrock was fixed at 2.44 m (96 in). A fixed pavement modulus value was used, based on laboratory measurements of dynamic modulus value. This was 3584.6 MPa (519.9 ksi) at 21.1°C (70°F) and the measured asphalt temperatures were inserted into the data files (the measured temperature was 18.9°C , or 66°F , on both days).

Table 10. Back-calculated modulus values based on FWD tests and the ELMOD program.

Test Section	Subgrade modulus (MPa/ ksi)		Base modulus (MPa/ ksi)	
	12/2/05	5/15/06	12/2/05	5/15/06
1	118.6/ 17.2	60.0/ 8.7	221.3/ 32.1	211.0/ 30.6
2	137.9/ 20.0	56.5/ 8.2	121.4/ 17.6	110.3/ 16.0
3	108.3/ 15.7	54.5/ 7.9	335.8/ 48.7	281.3/ 40.8
4	113.8/ 16.5	52.4/ 7.6	182.0/ 26.4	109.9/ 15.9
5	111.0/ 16.1	57.2/ 8.3	317.9/ 46.1	200.6/ 29.1
6	133.1/ 19.3	60.0/ 8.7	261.3/ 37.9	188.9/ 27.4
7	124.8/ 18.1	79.3/ 11.5	346.1/ 50.2	302.7/ 43.9
8	133.1/ 19.3	77.9/ 11.3	328.2/ 47.6	277.2/ 40.2

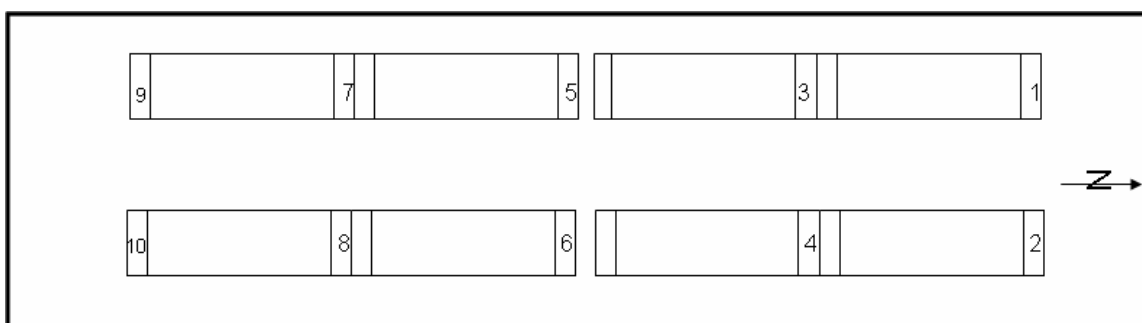


Figure 31. Plan view showing test area, test sections and FWD points (labeled 1 through 10). The FWD points 1 through 8 are on the northern transition zone of the test section labeled with the same number.

CONCLUSION

A set of full-scale pavement test sections was constructed and instrumented as a part of a national pooled-fund study to evaluate the reinforcing effect of a geogrid placed between the base and subgrade layers of pavement typically constructed by state transportation agencies. Prior studies reported significant benefits related to the presence of a geogrid layer with soft subgrades and relatively thin asphalt layers compared to typical state highways, and the test sections were constructed for this study to help evaluate the potential benefits of geogrid reinforcement in pavement structures representative of modern highways. The testing of the pavement test sections included accelerated pavement testing by means of a heavy vehicle simulator under controlled temperature and moisture conditions.

Subsequent publications will present the accelerated traffic test results, including the pavement response in terms of stress and strain, and the pavement performance in terms of permanent deformation and other forms of distress observed. Analyses of the test results will provide the basis for the development of pavement models compatible

with future modifications to NCHRP 1-37A, Guide for Mechanistic-Empirical Design of New and Rehabilitated Pavement Structures, currently available from <http://www.trb.org/mepdg/>.

ACKNOWLEDGEMENTS

The authors acknowledge the sponsorship by the Federal Highway Administration (FHWA), and the participating state transportation agencies. In particular, the leadership and encouragement of the Maine Department of Transportation is greatly appreciated. The authors express special gratitude to Professors Dana Humphrey and William Davids of the University of Maine and Mr. Dale Peabody from Maine Department of Transportation for their advice throughout this research project.

REFERENCES

AASHTO-T 180 Moisture-Density Relations of Soils Using a (4.55-kg) 10-lb Rammer and an (457-mm) 18-in. Drop (Modified Proctor). American Association for State Highway and Transportation Officials.

AASHTO-T 307-99 Standard test method for determining the resilient modulus of soils and aggregate materials. American Association for State Highway and Transportation Officials.

ASTM D 2937-04 Standard Test Method for Density of soil in place by the drive-cylinder method, ASTM International, West Conshohocken, PA.

ASTM D 6637-01 Standard Test Method for Determining Tensile Properties of Geogrids by the Single or Multi-Rib Tensile Method, ASTM International, West Conshohocken, PA.

Clapp, J. (2007) Analysis of rutting development in flexible pavements with geogrid reinforced base layers using 3D finite element analysis. Master's Thesis, University of Maine-Orono, Orono, ME. 211 p.

Clegg, B., (1986) Correlation with California Bearing Ratio, Clegg, Ltd. Newsletter No. 2, July.

Dynatest International, Elmod 5.0 Quick Start Manual, Dynatest International, Stark, FL 35 p.

Helmstrom, C. L., D.N. Humphrey and J.M. Labbe (2006), Performance and effectiveness of a thin pavement section using geogrids and drainage geocomposites in a cold region, NETCR60, NETC Project No. 00-8, Prepared for the New England Transportation Consortium, 263 p.

Janoo, V., Lynn Irwin and R. Haehnel (2003), Pavement subgrade performance study: Project overview, ERDC/CRREL Technical Report 03-05, U.S. Army Engineer Research and Development Center, Cold Regions Research and Engineering Laboratory, Hanover, NH, 79 p.

Perkins, S.W. and E.R. Cortez (2005), Evaluation of base-reinforced pavements using a heavy vehicle simulator, Geosynthetics International, Volume 12, No. 2, pp. 86-98.

Perkins and Ismeik (1997), A synthesis and evaluation of geosynthetic-reinforced bases in flexible pavements: Part I, Geosynthetics International, Volume 4, No. 6, pp. 549-604.

Vischer, W. (2003), Low-Volume Road Flexible Pavement Design with Geogrid-Reinforced Base, Transportation Research Record 1819, Washington, D.C.

Webster, S.L., R.H. Grau, and T.P. Williams (1992) Description and application of dual mass dynamic cone penetrometer. USACE Waterways Experimental Station, Vicksburg, Mississippi, Instruction Report GL-92-3.

APPENDIX A

INSTRUMENTATION LOCATIONS IN EACH TEST SECTION

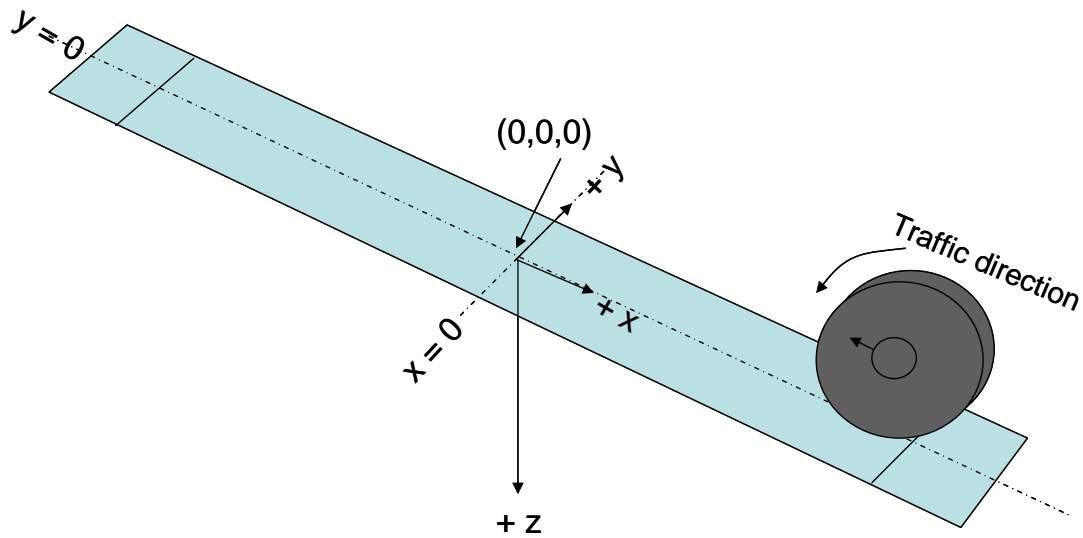


Figure A.1. Local coordinate system for each test section.

Tables A1.a through h document the locations of the thermocouples. Test windows are defined as the area where traffic is applied (includes wheel wander). Five thermocouples were installed in each test section. Two sensors were located in the subgrade at two different depths. One sensor is located in the middle of the base course. One sensor is located in the middle of the asphalt concrete, and one sensor is located in the air 0.91 m (3 ft) above the asphalt surface to monitor the air temperature.

Table A1.a. Location of Thermocouples in Test Section 1.

ID*	Location		
	X(mm/ in)	Y(mm/ in)	Z(mm/ in)
W1-T1	2134/ 84	0/ 0	305/ 12
W1-T2	2134/ 84	0/ 0	495/ 19.5
W1-T3	2134/ 84	0/ 0	1295/ 51
W1-T4	2134/ 84	0/ 0	76/ 3
W1-T5	2134/ 84	1981/ 78	-914/ -36
*W = Window T=Thermocouple			

Table A1.b. Location of Thermocouples in Test Section 2.

ID*	Location		
	X(mm/ in)	Y(mm/ in)	Z(mm/ in)
W2-T1	2134/ 84	0/ 0	254/ 10
W2-T2	2134/ 84	0/ 0	445/ 17.5
W2-T3	2134/ 84	0/ 0	1245/ 49
W2-T4	2134/ 84	0/ 0	51/ 2
W2-T5	2134/ 84	-4420/ -174	-914/ -36
<i>*W = Window T=Thermocouple</i>			

Table A1.c. Location of Thermocouples in Test Section 3.

ID*	Location		
	X(mm/ in)	Y(mm/ in)	Z(mm/ in)
W3-T1	2134/ 84	0/ 0	305/ 12
W3-T2	2134/ 84	0/ 0	495/ 19.5
W3-T3	2134/ 84	0/ 0	1295/ 51
W3-T4	2134/ 84	0/ 0	76/ 3
W3-T5	2134/ 84	1981/ 78	-914/ -36
<i>*W = Window T=Thermocouple</i>			

Table A1.d. Location of Thermocouples in Test Section 4.

ID*	Location		
	X(mm/ in)	Y(mm/ in)	Z(mm/ in)
W4-T1	2134/ 84	0/ 0	305/ 12
W4-T2	2134/ 84	0/ 0	495/ 19.5
W4-T3	2134/ 84	0/ 0	1295/ 51
W4-T4	2134/ 84	0/ 0	76/ 3
W4-T5	2134/ 84	-4420/ -174	-914/ -36
<i>*W = Window T=Thermocouple</i>			

Table A1.e. Location of Thermocouples in Test Section 5.

ID*	Location		
	X(mm/ in)	Y(mm/ in)	Z(mm/ in)
W5-T1	2134/ 84	0/ 0	457/ 18
W5-T2	2134/ 84	0/ 0	800/ 31.5
W5-T3	2134/ 84	0/ 0	1295/ 51
W5-T4	2134/ 84	0/ 0	76/ 3
W5-T5	2134/ 84	1981/ 78	-914/ -36
<i>*W = Window T=Thermocouple</i>			

Table A1.f. Location of Thermocouples in Test Section 6.

ID*	Location		
	X(mm/ in)	Y(mm/ in)	Z(mm/ in)
W6-T1	2134/ 84	0/ 0	406/ 16
W6-T2	2134/ 84	0/ 0	749/ 29.5
W6-T3	2134/ 84	0/ 0	1245/ 49
W6-T4	2134/ 84	0/ 0	76/ 3
W6-T5	2134/ 84	-4420/ -174	-914/ -36
<i>*W = Window T=Thermocouple</i>			

Table A1.g. Location of Thermocouples in Test Section 7.

ID*	Location		
	X(mm/ in)	Y(mm/ in)	Z(mm/ in)
W7-T1	2134/ 84	0/ 0	457/ 18
W7-T2	2134/ 84	0/ 0	800/ 31.5
W7-T3	2134/ 84	0/ 0	1295/ 51
W7-T4	2134/ 84	0/ 0	76/ 3
W7-T5	2134/ 84	1981/ 78	-914/ -36
<i>*W = Window T=Thermocouple</i>			

Table A1.h. Location of Thermocouples in Test Section 8.

ID*	Location		
	X(mm/ in)	Y(mm/ in)	Z(mm/ in)
W8-T1	2134/ 84	0/ 0	406/ 16
W8-T2	2134/ 84	0/ 0	749/ 29.5
W8-T3	2134/ 84	0/ 0	1245/ 49
W8-T4	2134/ 84	0/ 0	76/ 3
W8-T5	2134/ 84	-4420/ -174	-914/ -36
<i>*W = Window T=Thermocouple</i>			

Table A2.a. Location of Moisture Sensors in Test Section 1.

ID*	Location		
	X(mm/ in)	Y(mm/ in)	Z(mm/ in)
W1-M1	2134/ 84	0/ 0	305/ 12
W1-M2	2134/ 84	0/ 0	495/ 19.5
W1-M3	2134/ 84	0/ 0	1295/ 51
<i>*W = Window M=Moisture sensor</i>			

Table A2.b. Location of Moisture Sensors in Test Section 2.

ID*	Location		
	X(mm/ in)	Y(mm/ in)	Z(mm/ in)
W2-M1	2134/ 84	0/ 0	254/ 10
W2-M2	2134/ 84	0/ 0	445/ 17.5
W2-M3	2134/ 84	0/ 0	1295/ 51
<i>*W = Window M=Moisture sensor</i>			

Table A2.c. Location of Moisture Sensors in Test Section 3.

ID*	Location		
	X(mm/ in)	Y(mm/ in)	Z(mm/ in)
W3-M1	2134/ 84	0/ 0	305/ 12
W3-M2	2134/ 84	0/ 0	495/ 19.5
W3-M3	2134/ 84	0/ 0	1295/ 51
<i>*W = Window M=Moisture sensor</i>			

Table A2.d. Location of Moisture Sensors in Test Section 4.

ID*	Location		
	X(mm/ in)	Y(mm/ in)	Z(mm/ in)
W4-M1	2134/ 84	0/ 0	254/ 10
W4-M2	2134/ 84	0/ 0	445/ 17.5
W4-M3	2134/ 84	0/ 0	1295/ 51
<i>*W = Window M=Moisture sensor</i>			

Table A2.e. Location of Moisture Sensors in Test Section 5.

ID*	Location		
	X(mm/ in)	Y(mm/ in)	Z(mm/ in)
W5-M1	2134/ 84	0/ 0	457/ 18
W5-M2	2134/ 84	0/ 0	800/ 31.5
W5-M3	2134/ 84	0/ 0	1295/ 51
<i>*W = Window M=Moisture sensor</i>			

Table A2.f. Location of Moisture Sensors in Test Section 6.

ID*	Location		
	X(mm/ in)	Y(mm/ in)	Z(mm/ in)
W6-M1	2134/ 84	0/ 0	406/ 16
W6-M2	2134/ 84	0/ 0	749/ 29.5
W6-M3	2134/ 84	0/ 0	1295/ 51
<i>*W = Window M=Moisture sensor</i>			

Table A2.g. Location of Moisture Sensors in Test Section 7.

ID*	Location		
	X(mm/ in)	Y(mm/ in)	Z(mm/ in)
W7-M1	2134/ 84	0/ 0	457/ 18
W7-M2	2134/ 84	0/ 0	800/ 31.5
W7-M3	2134/ 84	0/ 0	1295/ 51
<i>*W = Window M=Moisture sensor</i>			

Table A2.h. Location of Moisture Sensors in Test Section 8.

ID*	Location		
	X(mm/ in)	Y(mm/ in)	Z(mm/ in)
W8-M1	2134/ 84	0/ 0	406/ 16
W8-M2	2134/ 84	0/ 0	749/ 29.5
W8-M3	2134/ 84	0/ 0	1295/ 51
<i>*W = Window M=Moisture sensor</i>			

Table A3.a. Location of stress sensors in Test Section 1.

ID*	Direction	Location		
		X(mm/ in)	Y(mm/ in)	Z(mm/ in)
W1-G11	Vertical	-457/ -18	0/ 0	229/ 9
W1-G12	Longitudinal	-1067/ -42	0/ 0	229/ 9
W1-G13	Transverse	-1067/ -42	-152/ -6	229/ 9
W1-G21	Vertical	-457/ -18	0/ 0	533/ 21
W1-G22	Longitudinal	-1067/ -42	0/ 0	533/ 21
W1-G23	Transverse	-1067/ -42	-152/ -6	533/ 21
W1-G31	Vertical	-457/ -18	0/ 0	1295/ 51
<i>*W = Window G=Stress sensor</i>				

Table A3.b. Location of stress sensors in Test Section 2.

ID*	Direction	Location		
		X(mm/ in)	Y(mm/ in)	Z(mm/ in)
W2-G11	Vertical	-457/ -18	0/ 0	178/ 7
W2-G12	Longitudinal	-1067/ -42	0/ 0	178/ 7
W2-G13	Transverse	-1067/ -42	-152/ -6	178/ 7
W2-G21	Vertical	-457/ -18	0/ 0	483/ 19
W2-G22	Longitudinal	-1067/ -42	0/ 0	483/ 19
W2-G23	Transverse	-1067/ -42	-152/ -6	483/ 19
W2-G31	Vertical	-457/ -18	0/ 0	1245/ 49
<i>*W = Window G=Stress sensor</i>				

Table A3.c. Location of stress sensors in Test Section 3.

ID*	Direction	Location		
		X(mm/ in)	Y(mm/ in)	Z(mm/ in)
W3-G11	Vertical	-457/ -18	0/ 0	229/ 9
W3-G12	Longitudinal	-1067/ -42	0/ 0	229/ 9
W3-G13	Transverse	-1067/ -42	-152/ -6	229/ 9
W3-G21	Vertical	-457/ -18	0/ 0	533/ 21
W3-G22	Longitudinal	-1067/ -42	0/ 0	533/ 21
W3-G23	Transverse	-1067/ -42	-152/ -6	533/ 21
W3-G31	Vertical	-457/ -18	0/ 0	1295/ 51
<i>*W = Window G=Stress sensor</i>				

Table A3.d. Location of stress sensors in Test Section 4.

ID*	Direction	Location		
		X(mm/ in)	Y(mm/ in)	Z(mm/ in)
W4-G11	Vertical	-457/ -18	0/ 0	178/ 7
W4-G12	Longitudinal	-1067/ -42	0/ 0	178/ 7
W4-G13	Transverse	-1067/ -42	-152/ -6	178/ 7
W4-G21	Vertical	-457/ -18	0/ 0	483/ 19
W4-G22	Longitudinal	-1067/ -42	0/ 0	483/ 19
W4-G23	Transverse	-1067/ -42	-152/ -6	483/ 19
W4-G31	Vertical	-457/ -18	0/ 0	1245/ 49
<i>*W = Window G=Stress sensor</i>				

Table A3.e. Location of stress sensors in Test Section 5.

ID*	Direction	Location		
		X(mm/ in)	Y(mm/ in)	Z(mm/ in)
W5-G11	Vertical	-457/ -18	0/ 0	229/ 9
W5-G12	Longitudinal	-1067/ -42	0/ 0	229/ 9
W5-G13	Transverse	-1067/ -42	-152/ -6	229/ 9
W5-G21	Vertical	-457/ -18	0/ 0	838/ 33
W5-G22	Longitudinal	-1067/ -42	0/ 0	838/ 33
W5-G23	Transverse	-1067/ -42	-152/ -6	838/ 33
W5-G31	Vertical	-457/ -18	0/ 0	1295/ 51
<i>*W = Window G=Stress sensor</i>				

Table A3.f. Location of stress sensors in Test Section 6.

ID*	Direction	Location		
		X(mm/ in)	Y(mm/ in)	Z(mm/ in)
W6-G11	Vertical	-457/ -18	0/ 0	178/ 7
W6-G12	Longitudinal	-1067/ -42	0/ 0	178/ 7
W6-G13	Transverse	-1067/ -42	-152/ -6	178/ 7
W6-G21	Vertical	-457/ -18	0/ 0	787/ 31
W6-G22	Longitudinal	-1067/ -42	0/ 0	787/ 31
W6-G23	Transverse	-1067/ -42	-152/ -6	787/ 31
W6-G31	Vertical	-457/ -18	0/ 0	1245/ 49
<i>*W = Window G=Stress sensor</i>				

Table A3.g. Location of stress sensors in Test Section 7.

ID*	Direction	Location		
		X(mm/ in)	Y(mm/ in)	Z(mm/ in)
W7-G11	Vertical	-457/ -18	0/ 0	229/ 9
W7-G12	Longitudinal	-1067/ -42	0/ 0	229/ 9
W7-G13	Transverse	-1067/ -42	-152/ -6	229/ 9
W7-G21	Vertical	-457/ -18	0/ 0	838/ 33
W7-G22	Longitudinal	-1067/ -42	0/ 0	838/ 33
W7-G23	Transverse	-1067/ -42	-152/ -6	838/ 33
W7-G31	Vertical	-457/ -18	0/ 0	1295/ 51
<i>*W = Window G=Stress sensor</i>				

Table A3.h. Location of stress sensors in Test Section 8.

ID*	Direction	Location		
		X(mm/ in)	Y(mm/ in)	Z(mm/ in)
W8-G11	Vertical	-457/ -18	0/ 0	178/ 7
W8-G12	Longitudinal	-1067/ -42	0/ 0	178/ 7
W8-G13	Transverse	-1067/ -42	-152/ -6	178/ 7
W8-G21	Vertical	-457/ -18	0/ 0	787/ 31
W8-G22	Longitudinal	-1067/ -42	0/ 0	787/ 31
W8-G23	Transverse	-1067/ -42	-152/ -6	787/ 31
W8-G31	Vertical	-457/ -18	0/ 0	1245/ 49
<i>*W = Window G=Stress sensor</i>				

Table A4.a. Location of soil and asphalt strain sensors in Test Section 1.

ID*	Direction	Location		
		X(mm/ in)	Y(mm/ in)	Z(mm/ in)
W1-E1	Z	457/ 18	0/ 0	140/ 5.5
W1-E4	Z	457/ 18	0/ 0	305/ 12
W1-E7	Z	457/ 18	0/ 0	470/ 18.5
W1-E10	Z	457/ 18	0/ 0	610/ 24
W1-E13	Z	457/ 18	0/ 0	762/ 30
W1-E16	Z	457/ 18	0/ 0	914/ 36
W1-E19	Z	457/ 18	0/ 0	1067/ 42
W1-E22	Z	457/ 18	0/ 0	1219/ 48
W1-E23	Z	457/ 18	0/ 0	1372/ 54
W1-E24	Z	457/ 18	0/ 0	1524/ 60
W1-E25	Z	457/ 18	0/ 0	1676/ 66
W1-E2	X	610/ 24	0/ 0	140/ 5.5
W1-E5	X	610/ 24	0/ 0	305/ 12
W1-E8	X	610/ 24	0/ 0	470/ 18.5
W1-E11	X	610/ 24	0/ 0	610/ 24
W1-E14	X	610/ 24	0/ 0	762/ 30
W1-E17	X	610/ 24	0/ 0	914/ 36
W1-E20	X	610/ 24	0/ 0	1067/ 42
W1-E3	Y	457/ 18	152/ 6	140/ 5.5
W1-E6	Y	457/ 18	152/ 6	305/ 12
W1-E9	Y	457/ 18	152/ 6	470/ 18.5
W1-E12	Y	457/ 18	152/ 6	610/ 24
W1-E15	Y	457/ 18	152/ 6	762/ 30
W1-E18	Y	457/ 18	152/ 6	914/ 36
W1-E21	Y	457/ 18	152/ 6	1067/ 42
W1-E26	Z	0/ 0	0/ 0	140/ 5.5
W1-E27	X	152/ 6	0/ 0	140/ 5.5
W1-E28	Y	0/ 0	152/ 6	140/ 5.5
<i>*W = Test section (Window) E=Emu sensor</i>				

Table A4.b. Location of soil and asphalt strain sensors in Test Section 2.

ID*	Direction	Location		
		X(mm/ in)	Y(mm/ in)	Z(mm/ in)
W2-E1	Z	457/ 18	0/ 0	89/ 3.5
W2-E4	Z	457/ 18	0/ 0	254/ 10
W2-E7	Z	457/ 18	0/ 0	419/ 16.5
W2-E10	Z	457/ 18	0/ 0	559/ 22
W2-E13	Z	457/ 18	0/ 0	711/ 28
W2-E16	Z	457/ 18	0/ 0	864/ 34
W2-E19	Z	457/ 18	0/ 0	1016/ 40
W2-E22	Z	457/ 18	0/ 0	1168/ 46
W2-E23	Z	457/ 18	0/ 0	1321/ 52
W2-E24	Z	457/ 18	0/ 0	1473/ 58
W2-E25	Z	457/ 18	0/ 0	1626/ 64
W2-E2	X	610/ 24	0/ 0	89/ 3.5
W2-E5	X	610/ 24	0/ 0	254/ 10
W2-E8	X	610/ 24	0/ 0	419/ 16.5
W2-E11	X	610/ 24	0/ 0	559/ 22
W2-E14	X	610/ 24	0/ 0	711/ 28
W2-E17	X	610/ 24	0/ 0	864/ 34
W2-E20	X	610/ 24	0/ 0	1016/ 40
W2-E3	Y	457/ 18	152/ 6	89/ 3.5
W2-E6	Y	457/ 18	152/ 6	254/ 10
W2-E9	Y	457/ 18	152/ 6	419/ 16.5
W2-E12	Y	457/ 18	152/ 6	559/ 22
W2-E15	Y	457/ 18	152/ 6	711/ 28
W2-E18	Y	457/ 18	152/ 6	864/ 34
W2-E21	Y	457/ 18	152/ 6	1016/ 40
W2-E26	Z	0/ 0	0/ 0	89/ 3.5
W2-E27	X	152/ 6	0/ 0	89/ 3.5
W2-E28	Y	0/ 0	152/ 6	89/ 3.5
<i>*W = Test section (Window) E=Emu sensor</i>				

Table A4.c. Location of soil and asphalt strain sensors in Test Section 3.

ID*	Direction	Location		
		X(mm/ in)	Y(mm/ in)	Z(mm/ in)
W3-E1	Z	457/ 18	0/ 0	140/ 5.5
W3-E4	Z	457/ 18	0/ 0	305/ 12
W3-E7	Z	457/ 18	0/ 0	470/ 18.5
W3-E10	Z	457/ 18	0/ 0	610/ 24
W3-E13	Z	457/ 18	0/ 0	762/ 30
W3-E16	Z	457/ 18	0/ 0	914/ 36
W3-E19	Z	457/ 18	0/ 0	1067/ 42
W3-E22	Z	457/ 18	0/ 0	1219/ 48
W3-E23	Z	457/ 18	0/ 0	1372/ 54
W3-E24	Z	457/ 18	0/ 0	1524/ 60
W3-E25	Z	457/ 18	0/ 0	1676/ 66
W3-E2	X	610/ 24	0/ 0	140/ 5.5
W3-E5	X	610/ 24	0/ 0	305/ 12
W3-E8	X	610/ 24	0/ 0	470/ 18.5
W3-E11	X	610/ 24	0/ 0	610/ 24
W3-E14	X	610/ 24	0/ 0	762/ 30
W3-E17	X	610/ 24	0/ 0	914/ 36
W3-E20	X	610/ 24	0/ 0	1067/ 42
W3-E3	Y	457/ 18	152/ 6	140/ 5.5
W3-E6	Y	457/ 18	152/ 6	305/ 12
W3-E9	Y	457/ 18	152/ 6	470/ 18.5
W3-E12	Y	457/ 18	152/ 6	610/ 24
W3-E15	Y	457/ 18	152/ 6	762/ 30
W3-E18	Y	457/ 18	152/ 6	914/ 36
W3-E21	Y	457/ 18	152/ 6	1067/ 42
W3-E26	Z	0/ 0	0/ 0	140/ 5.5
W3-E27	X	152/ 6	0/ 0	140/ 5.5
W3-E28	Y	0/ 0	152/ 6	140/ 5.5
<i>*W = Test section (Window) E=Emu sensor</i>				

Table A4.d. Location of soil and asphalt strain sensors in Test Section 4.

ID*	Direction	Location		
		X(mm/ in)	Y(mm/ in)	Z(mm/ in)
W4-E1	Z	457/ 18	0/ 0	89/ 3.5
W4-E4	Z	457/ 18	0/ 0	254/ 10
W4-E7	Z	457/ 18	0/ 0	419/ 16.5
W4-E10	Z	457/ 18	0/ 0	559/ 22
W4-E13	Z	457/ 18	0/ 0	711/ 28
W4-E16	Z	457/ 18	0/ 0	864/ 34
W4-E19	Z	457/ 18	0/ 0	1016/ 40
W4-E22	Z	457/ 18	0/ 0	1168/ 46
W4-E23	Z	457/ 18	0/ 0	1321/ 52
W4-E24	Z	457/ 18	0/ 0	1473/ 58
W4-E25	Z	457/ 18	0/ 0	1626/ 64
W4-E2	X	610/ 24	0/ 0	89/ 3.5
W4-E5	X	610/ 24	0/ 0	254/ 10
W4-E8	X	610/ 24	0/ 0	419/ 16.5
W4-E11	X	610/ 24	0/ 0	559/ 22
W4-E14	X	610/ 24	0/ 0	711/ 28
W4-E17	X	610/ 24	0/ 0	864/ 34
W4-E20	X	610/ 24	0/ 0	1016/ 40
W4-E3	Y	457/ 18	152/ 6	89/ 3.5
W4-E6	Y	457/ 18	152/ 6	254/ 10
W4-E9	Y	457/ 18	152/ 6	419/ 16.5
W4-E12	Y	457/ 18	152/ 6	559/ 22
W4-E15	Y	457/ 18	152/ 6	711/ 28
W4-E18	Y	457/ 18	152/ 6	864/ 34
W4-E21	Y	457/ 18	152/ 6	1016/ 40
W4-E26	Z	0/ 0	0/ 0	89/ 3.5
W4-E27	X	152/ 6	0/ 0	89/ 3.5
W4-E28	Y	0/ 0	152/ 6	89/ 3.5
<i>*W = Test section (Window) E=Emu sensor</i>				

Table A4.e. Location of soil and asphalt strain sensors in Test Section 5.

ID*	Direction	Location		
		X(mm/ in)	Y(mm/ in)	Z(mm/ in)
W5-E1	Z	457/ 18	0/ 0	140/ 5.5
W5-E4	Z	457/ 18	0/ 0	305/ 12
W5-E7	Z	457/ 18	0/ 0	470/ 18.5
W5-E10	Z	457/ 18	0/ 0	610/ 24
W5-E13	Z	457/ 18	0/ 0	762/ 30
W5-E16	Z	457/ 18	0/ 0	914/ 36
W5-E19	Z	457/ 18	0/ 0	1067/ 42
W5-E22	Z	457/ 18	0/ 0	1219/ 48
W5-E23	Z	457/ 18	0/ 0	1372/ 54
W5-E24	Z	457/ 18	0/ 0	1524/ 60
W5-E25	Z	457/ 18	0/ 0	1676/ 66
W5-E2	X	610/ 24	0/ 0	140/ 5.5
W5-E5	X	610/ 24	0/ 0	305/ 12
W5-E8	X	610/ 24	0/ 0	470/ 18.5
W5-E11	X	610/ 24	0/ 0	610/ 24
W5-E14	X	610/ 24	0/ 0	762/ 30
W5-E17	X	610/ 24	0/ 0	914/ 36
W5-E20	X	610/ 24	0/ 0	1067/ 42
W5-E3	Y	457/ 18	152/ 6	140/ 5.5
W5-E6	Y	457/ 18	152/ 6	305/ 12
W5-E9	Y	457/ 18	152/ 6	470/ 18.5
W5-E12	Y	457/ 18	152/ 6	610/ 24
W5-E15	Y	457/ 18	152/ 6	762/ 30
W5-E18	Y	457/ 18	152/ 6	914/ 36
W5-E21	Y	457/ 18	152/ 6	1067/ 42
W5-E26	Z	0/ 0	0/ 0	140/ 5.5
W5-E27	X	152/ 6	0/ 0	140/ 5.5
W5-E28	Y	0/ 0	152/ 6	140/ 5.5
<i>*W = Test section (Window) E=Emu sensor</i>				

Table A4.f. Location of soil and asphalt strain sensors in Test Section 6.

ID*	Direction	Location		
		X(mm/ in)	Y(mm/ in)	Z(mm/ in)
W6-E1	Z	457/ 18	0/ 0	89/ 3.5
W6-E4	Z	457/ 18	0/ 0	254/ 10
W6-E7	Z	457/ 18	0/ 0	406/ 16
W6-E10	Z	457/ 18	0/ 0	559/ 22
W6-E13	Z	457/ 18	0/ 0	724/ 28.5
W6-E16	Z	457/ 18	0/ 0	864/ 34
W6-E19	Z	457/ 18	0/ 0	1016/ 40
W6-E22	Z	457/ 18	0/ 0	1168/ 46
W6-E23	Z	457/ 18	0/ 0	1321/ 52
W6-E24	Z	457/ 18	0/ 0	1473/ 58
W6-E25	Z	457/ 18	0/ 0	1626/ 64
W6-E2	X	610/ 24	0/ 0	89/ 3.5
W6-E5	X	610/ 24	0/ 0	254/ 10
W6-E8	X	610/ 24	0/ 0	406/ 16
W6-E11	X	610/ 24	0/ 0	559/ 22
W6-E14	X	610/ 24	0/ 0	724/ 28.5
W6-E17	X	610/ 24	0/ 0	864/ 34
W6-E20	X	610/ 24	0/ 0	1016/ 40
W6-E3	Y	457/ 18	152/ 6	89/ 3.5
W6-E6	Y	457/ 18	152/ 6	254/ 10
W6-E9	Y	457/ 18	152/ 6	406/ 16
W6-E12	Y	457/ 18	152/ 6	559/ 22
W6-E15	Y	457/ 18	152/ 6	724/ 28.5
W6-E18	Y	457/ 18	152/ 6	864/ 34
W6-E21	Y	457/ 18	152/ 6	1016/ 40
W6-E26	Z	0/ 0	0/ 0	89/ 3.5
W6-E27	X	152/ 6	0/ 0	89/ 3.5
W6-E28	Y	0/ 0	152/ 6	89/ 3.5
<i>*W = Test section (Window) E=Emu sensor</i>				

Table A4.g. Location of soil and asphalt strain sensors in Test Section 7.

ID*	Direction	Location		
		X(mm/ in)	Y(mm/ in)	Z(mm/ in)
W7-E1	Z	457/ 18	0/ 0	140/ 5.5
W7-E4	Z	457/ 18	0/ 0	305/ 12
W7-E7	Z	457/ 18	0/ 0	457/18
W7-E10	Z	457/ 18	0/ 0	610/ 24
W7-E13	Z	457/ 18	0/ 0	775/30.5
W7-E16	Z	457/ 18	0/ 0	914/ 36
W7-E19	Z	457/ 18	0/ 0	1067/ 42
W7-E22	Z	457/ 18	0/ 0	1219/ 48
W7-E23	Z	457/ 18	0/ 0	1372/ 54
W7-E24	Z	457/ 18	0/ 0	1524/ 60
W7-E25	Z	457/ 18	0/ 0	1676/ 66
W7-E2	X	610/ 24	0/ 0	140/ 5.5
W7-E5	X	610/ 24	0/ 0	305/ 12
W7-E8	X	610/ 24	0/ 0	457/18
W7-E11	X	610/ 24	0/ 0	610/ 24
W7-E14	X	610/ 24	0/ 0	775/30.5
W7-E17	X	610/ 24	0/ 0	914/ 36
W7-E20	X	610/ 24	0/ 0	1067/ 42
W7-E3	Y	457/ 18	152/ 6	140/ 5.5
W7-E6	Y	457/ 18	152/ 6	305/ 12
W7-E9	Y	457/ 18	152/ 6	457/18
W7-E12	Y	457/ 18	152/ 6	610/ 24
W7-E15	Y	457/ 18	152/ 6	775/30.5
W7-E18	Y	457/ 18	152/ 6	914/ 36
W7-E21	Y	457/ 18	152/ 6	1067/ 42
W7-E26	Z	0/ 0	0/ 0	140/ 5.5
W7-E27	X	152/ 6	0/ 0	140/ 5.5
W7-E28	Y	0/ 0	152/ 6	140/ 5.5
<i>*W = Test section (Window) E=Emu sensor</i>				

Table A4.h. Location of soil and asphalt strain sensors in Test Section 8.

ID*	Direction	Location		
		X(mm/ in)	Y(mm/ in)	Z(mm/ in)
W8-E1	Z	457/ 18	0/ 0	89/ 3.5
W8-E4	Z	457/ 18	0/ 0	254/ 10
W8-E7	Z	457/ 18	0/ 0	406/ 16
W8-E10	Z	457/ 18	0/ 0	559/ 22
W8-E13	Z	457/ 18	0/ 0	724/ 28.5
W8-E16	Z	457/ 18	0/ 0	864/ 34
W8-E19	Z	457/ 18	0/ 0	1016/ 40
W8-E22	Z	457/ 18	0/ 0	1168/ 46
W8-E23	Z	457/ 18	0/ 0	1321/ 52
W8-E24	Z	457/ 18	0/ 0	1473/ 58
W8-E25	Z	457/ 18	0/ 0	1626/ 64
W8-E2	X	610/ 24	0/ 0	89/ 3.5
W8-E5	X	610/ 24	0/ 0	254/ 10
W8-E8	X	610/ 24	0/ 0	406/ 16
W8-E11	X	610/ 24	0/ 0	559/ 22
W8-E14	X	610/ 24	0/ 0	724/ 28.5
W8-E17	X	610/ 24	0/ 0	864/ 34
W8-E20	X	610/ 24	0/ 0	1016/ 40
W8-E3	Y	457/ 18	152/ 6	89/ 3.5
W8-E6	Y	457/ 18	152/ 6	254/ 10
W8-E9	Y	457/ 18	152/ 6	406/ 16
W8-E12	Y	457/ 18	152/ 6	559/ 22
W8-E15	Y	457/ 18	152/ 6	724/ 28.5
W8-E18	Y	457/ 18	152/ 6	864/ 34
W8-E21	Y	457/ 18	152/ 6	1016/ 40
W8-E26	Z	0/ 0	0/ 0	89/ 3.5
W8-E27	X	152/ 6	0/ 0	89/ 3.5
W8-E28	Y	0/ 0	152/ 6	89/ 3.5
<i>*W = Test section (Window) E=Emu sensor</i>				

Table A5.a. Location of geogrid strain gages in Test Section 3.

ID*	Direction	Location		Top/Bottom
		X(mm/ in)	Y(mm/ in)	
W3-S1	Transverse	-916/ -36	-305/ -12	Top
W3-S2	Transverse	-916/ -36	-305/ -12	Bottom
W3-S3	Transverse	-1219/ -48	0/ 0	Top
W3-S4	Transverse	-1219/ -48	0/ 0	Bottom
W3-S5	Longitudinal	-1524/ -60	0/ 0	Top
W3-S6	Longitudinal	-1524/ -60	0/ 0	Bottom
W3-S7	Transverse	-1829/ -72	0/ 0	Top
W3-S8	Transverse	-1829/ -72	0/ 0	Bottom
W3-S9	Transverse	-2134/ -84	305/ 12	Top
W3-S10	Transverse	-2134/ -84	305/ 12	Bottom
* W = Window S = Strain gage				

Table A5.b. Location of geogrid strain gages in Test Section 4.

ID*	Direction	Location		Top/Bottom
		X(in)	Y(in)	
W4-S1	Transverse	-916/ -36	-305/ -12	Top
W4-S2	Transverse	-916/ -36	-305/ -12	Bottom
W4-S3	Transverse	-1219/ -48	0/ 0	Top
W4-S4	Transverse	-1219/ -48	0/ 0	Bottom
W4-S5	Longitudinal	-1524/ -60	0/ 0	Top
W4-S6	Longitudinal	-1524/ -60	0/ 0	Bottom
W4-S7	Transverse	-1829/ -72	0/ 0	Top
W4-S8	Transverse	-1829/ -72	0/ 0	Bottom
W4-S9	Transverse	-2134/ -84	305/ 12	Top
W4-S10	Transverse	-2134/ -84	305/ 12	Bottom
<i>* W = Window S = Strain gage</i>				

Table A5.c. Location of geogrid strain gages in Test Section 7.

ID*	Direction	Location		Top/Bottom
		X(in)	Y(in)	
W7-S1	Transverse	-916/ -36	-305/ -12	Top
W7-S2	Transverse	-916/ -36	-305/ -12	Bottom
W7-S3	Transverse	-1219/ -48	0/ 0	Top
W7-S4	Transverse	-1219/ -48	0/ 0	Bottom
W7-S5	Longitudinal	-1524/ -60	0/ 0	Top
W7-S6	Longitudinal	-1524/ -60	0/ 0	Bottom
W7-S7	Transverse	-1829/ -72	0/ 0	Top
W7-S8	Transverse	-1829/ -72	0/ 0	Bottom
W7-S9	Transverse	-2134/ -84	305/ 12	Top
W7-S10	Transverse	-2134/ -84	305/ 12	Bottom
<i>* W = Window S = Strain gage</i>				

Table A5.d. Location of geogrid strain gages in Test Section 8.

ID*	Direction	Location		Top/Bottom
		X(in)	Y(in)	
W8-S1	Transverse	-916/ -36	-305/ -12	Top
W8-S2	Transverse	-916/ -36	-305/ -12	Bottom
W8-S3	Transverse	-1219/ -48	0/ 0	Top
W8-S4	Transverse	-1219/ -48	0/ 0	Bottom
W8-S5	Longitudinal	-1524/ -60	0/ 0	Top
W8-S6	Longitudinal	-1524/ -60	0/ 0	Bottom
W8-S7	Transverse	-1829/ -72	0/ 0	Top
W8-S8	Transverse	-1829/ -72	0/ 0	Bottom
W8-S9	Transverse	-2134/ -84	305/ 12	Top
W8-S10	Transverse	-2134/ -84	305/ 12	Bottom
* W = Window S = Strain gage				

APPENDIX B

**AS-BUILT SUBGRADE AND BASE COURSE MOISTURE
DETERMINED WITH TROXLER NUCLEAR GAGE**

Tables B1 and B2 document the gravimetric moisture content measured with the Troxler nuclear gage in the West and East ‘lanes’ of the test basin, respectively, while B3 and B4 document the dry density determinations of the West and East lanes. In the West lane (Test Sections 1, 3, 5 and 7), readings were taken along a line that was 0.3 m (1 ft) from the West edge of the traffic window. In the East lane, the line was only 0.15 m (0.5 ft) from the West edge of the traffic window. North readings were taken in the traffic window right at the line of transition where the full load is first applied. Middle readings were taken in the middle of the test window. South readings were taken in the traffic window right at the line of transition where the full load is first removed (Fig. B.1).

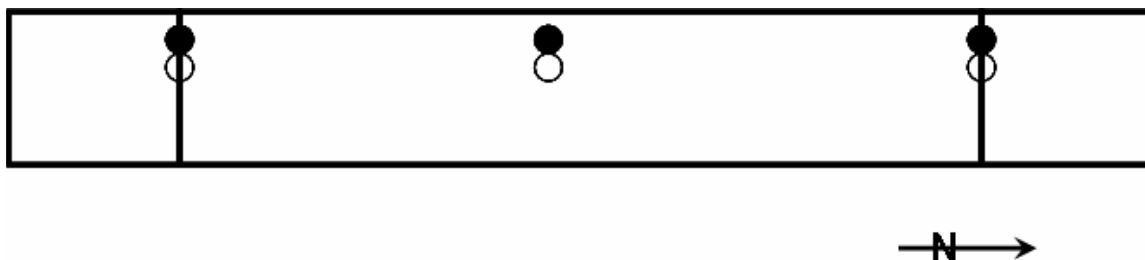


Figure B.1. Plan view image showing the locations of Troxler Nuclear Gage readings with respect to the traffic window of each test section (not to scale). The traffic load is fully applied in the center portion of the window and the two marked ends are the transition zones. The empty circles represent the reading locations for test windows 1, 3, 5 and 7 and the dark circles represent test windows 2, 4, 6 and 8.

Table B1. Base and subgrade moisture content in Test Sections 1, 3, 5 and 7, determined with the nuclear gage.*

Location	Test Section	1			3			5			7		
		North	Middle	South									
	Depth(in*)												
Top of Base	7	2.7	2.6	2.9	3.2	3.0	3.0	3.2	3.4	3.0	2.8	3.1	2.4
Base course	10	2.7	2.7	3.2	3.8	3.1	3.5	3.8	4.3	3.1	2.4	2.8	2.3
Base course	16-20							2.8	2.6	2.8	2.4	3.1	3.3
Base course	19							1.9	2.1	2.0	2.4	2.2	2.3
Subgrade	16-20	10.2	11.4	10.3	10.1	10.8	12.2						
Subgrade	25-30	12.3	12.0	12.9	12.0	11.7	12.4	11.3	11.6	10.9	11.6	10.8	10.1
Subgrade	31	12.8	12.4	13.1	13.3	13.0	12.7	12.8	13.2	13.3	12.8	12.1	12.5
Subgrade	37	12.9	12.3	11.3	12.4	11.9	12.4	12.2	12.4	12.6	12.8	12.0	12.0
Subgrade	43	11.8	11.9	11.6	13.1	12.9	11.4	12.7	12.5	11.0	11.7	11.0	9.7
Lower subgrade	117	13.6	6.2	11.0	8.9	10.0	8.5	9.3	8.6	14.5	10.2	8.1	12.4

1 inch = 2.54 cm.

Table B2. Base and subgrade gravimetric moisture content in Test Sections 2, 4, 6 and 8, determined with the nuclear gage.

Location	Test Section	2			4			6			8		
		North	Middle	South									
	Depth(in)												
Top of Base	7	2.5	2.9	2.8	2.6	2.9	2.6	2.8	3.4	2.8	3.0	3.5	3.0
Basecourse	10	2.3	2.1	2.4	2.0	2.6	2.9	2.9	2.8	2.7	2.9	3.7	4.7
Basecourse	16-20							2.1	3.4	3.1	3.1	3.3	2.5
Basecourse	19							2.2	2.5	2.5	2.3	2.1	2.0
Subgrade	16-20	12.5	12.4	12.4	11.7	12.0	12.4						
Subgrade	25-30	12.4	12.6	12.6	12.0	12.4	13.1	11.1	11.0	11.4	11.7	11.5	10.3
Subgrade	31	13.3	13.9	12.2	13.7	12.9	13.9	12.6	12.4	12.7	12.9	13.1	13.4
Subgrade	37	12.4	12.1	11.4	11.8	12.6	11.8	11.7	11.6	10.7	11.9	11.0	11.5
Subgrade	43	12.0	12.4	11.9	11.2	11.8	11.6	12.2	11.6	10.6	12.5	13.1	11.1
Lower subgrade	117	8.5	9.1	10.2	9.3	10.0	12.2	7.0	6.0	4.1	9.5	8.6	8.7

Table B3. Base and subgrade density ($\text{kg}\cdot\text{m}^{-3}$) in Test Sections 1, 3, 5 and 7, determined with a nuclear gage.

Location	Test Section	1			3			5			7		
	Depth (in*)	North	Middle	South									
Top of Base	7	2353/ 146.9	2361/ 147.4	2430/ 151.7	2281/ 142.4	2294/ 143.2	2272/ 141.8	2262/ 141.2	2198/ 137.2	2353/ 146.9	2336/ 145.8	2320/ 144.8	2268/ 141.6
Base course	10	2219/ 138.5	2193/ 136.9	2120/ 132.9	2216/ 138.3	2150/ 134.2	2244/ 140.1	2185/ 136.1	2111/ 131.8	2172/ 135.6	2357/ 147.1	2308/ 144.1	2244/ 140.1
Base course	16-20							2264/ 141.3	2262/ 141.2	2336/ 145.8	2278/ 142.2	2299/ 143.5	2328/ 145.3
Base course	19							2162/ 135.0	2041/ 127.4	2251/ 140.5	2353/ 146.9	2256/ 140.8	2275/ 142.0
Subgrade	16-20	1826/ 114.0	1826/ 114.0	1862/ 116.2	1850/ 115.5	1834/ 114.5	1831/ 114.3						
Subgrade	25-30	1884/ 117.6	1873/ 116.9	1890/ 118.0	1862/ 116.2	1911/ 119.3	1882/ 117.5	1897/ 118.4	1911/ 119.3	1894/ 118.2	1889/ 117.9	1913/ 119.4	1858/ 116.0
Subgrade	31	1847/ 115.3	1849/ 115.4	1852/ 115.6	1858/ 116.0	1882/ 117.5	1886/ 117.7	1876/ 117.1	1826/ 114.0	1828/ 114.1	1868/ 116.6	1882/ 117.5	1884/ 117.6
Subgrade	37	1829/ 114.2	1852/ 115.6	1882/ 117.5	1858/ 116.0	1863/ 116.3	1849/ 115.4	1854/ 115.7	1870/ 116.7	1846/ 115.2	1858/ 116.0	1862/ 116.2	1829/ 114.2
Subgrade	43	1834/ 114.5	1876/ 117.1	1837/ 114.7	1815/ 113.3	1846/ 115.2	1879/ 117.3	1829/ 114.2	1879/ 117.3	1863/ 116.3	1860/ 116.1	1764/ 110.1	1802/ 112.5
Lower subgrade	117	1849/ 115.4	1765/ 110.2	1783/ 111.3	1661/ 103.	1658/ 103.5	1653/ 103.2	1674/ 104.4	1684/ 105.1	1650/ 103.0	1778/ 111.0	1703/ 106.3	1650/ 103.0

Table B4. Base and subgrade density (kg-m³/ pcf) in Test Sections 2, 4, 6 and 8, determined with a nuclear gage.

Location	Test Section	2			4			6			8		
	Depth(in)	North	Middle	South									
Top of Base	7	2288/ 142.8	2337/ 145.9	2316/ 144.6	2342/ 146.2	2400/ 149.8	2288/ 142.8	2352/ 146.8	2382/ 148.7	2316/ 144.6	2310/ 144.2	2334/ 145.7	2272/ 141.8
Base course	10	2224/ 138.8	2143/ 133.8	2225/ 138.9	2185/ 136.4	2272/ 141.8	2302/ 143.7	2230/ 139.2	2195/ 137.0	2230/ 139.2	2344/ 146.3	2337/ 145.9	2318/ 144.7
Base course	16-20							2262/ 141.2	2344/ 146.3	2308/ 144.1	2280/ 142.3	2278/ 142.2	2333/ 145.6
Base course	19							2033/ 126.9	2214/ 138.2	2357/ 147.1	2240/ 139.8	2339/ 146.0	2325/ 145.1
Subgrade	16-20	1850/ 115.5	1833/ 114.4	1828/ 114.1	1829/ 114.2	1829/ 114.2	1831/ 114.3						
Subgrade	25-30	1826/ 114.0	1919/ 11938	1889/ 117.9	1929/ 120.4	1895/ 118.3	1826/ 114.0	1882/ 117.5	1970/ 123.0	1919/ 119.8	1910/ 119.2	1826/ 114.0	1850/ 115.5
Subgrade	31	1878/ 117.2	1876/ 117.1	1860/ 116.1	1829/ 114.2	1837/ 114.7	1828/ 114.1	1846/ 115.2	1833/ 114.4	1884/ 117.6	1863/ 116.3	1839/ 114.8	1828/ 114.1
Subgrade	37	1873/ 116.9	1826/ 114.0	1844/ 115.1	1863/ 116.3	1844/ 114.7	1913/ 119.4	1831/ 114.3	1898/ 118.5	1913/ 119.4	1868/ 116.6	1927/ 120.3	1882/ 117.5
Subgrade	43	1873/ 116.9	1846/ 115.2	1882/ 117.5	1839/ 114.8	1862/ 115.1	1849/ 115.4	1849/ 115.4	1754/ 109.5	1725/ 107.7	1868/ 116.6	1831/ 114.3	1820/ 113.6
Lower subgrade	117	1661/ 103.7	1729/ 107.9	1607/ 100.3	1695/ 105.8	1645/ 102.7	1596/ 99.6	1773/ 110.7	1852/ 115.6	1812/ 113.1	1666/ 104.0	1684/ 105.1	1656/ 103.4

APPENDIX C

CBR DETERMINATIONS AT THE TOP OF THE FINISHED SUBGRADE DETERMINED ACCORDING TO DYNAMIC CONE PENETROMETER AND CLEGG IMPACT HAMMER MEASUREMENTS

For each test section, dynamic cone penetrometer (DCP) measurements were made at three locations at approximately the center of a longitudinal line through the test window. North, Middle, and South refers to the transition lines (North and South) and center of the test window as shown in Figure B.1 above. The following relation was used to provide the estimates shown in Tables C1 through C8 (Webster, et al., 1992):

$$CBR(\%) = \frac{292}{\left(\frac{mm}{blow}\right)^{1.12}}$$

Raw DCP data used to make the determinations in Tables C1 through C8 is provided in Table C9.

Table C1. CBR estimates, based on DCP tests in Test Section 1.

Depth* (mm/ in)	North	Middle	South
0/ 0	10	14	11
305/ 12	22	37	36
610/ 24	26	24	24
914/ 36	12	12	12

* Depth was measured from top of subgrade.

Table C2. CBR estimates, based on DCP tests in Test Section 2.

Depth* (mm/ in)	North	Middle	South
0/ 0	12	14	10
305/ 12	36	37	40
610/ 24	38	28	38
914/ 36	14	19	11

* Depth was measured from top of subgrade.

Table C3. CBR estimates, based on DCP tests in Test Section 3.

Depth* (mm/ in)	North	Middle	South
0/ 0	11	13	9
305/ 12	36	44	43
610/ 24	24	25	20
914/ 36	12	19	11

* Depth was measured from top of subgrade.

Table C4. CBR estimates, based on DCP tests in Test Section 4.

Depth* (mm/ in)	North	Middle	South
0/ 0	10	13	12
305/ 12	40	43	36
610/ 24	38	30	36
914/ 36	11	24	24

* Depth was measured from top of subgrade.

Table C5. CBR estimates, based on DCP tests in Test Section 5.

Depth* (mm/ in)	North	Middle	South
0/ 0	12	22	9
305/ 12	26	17	43
610/ 24	18	14	20
914/ 36	16	37	11

* Depth was measured from top of subgrade.

Table C6. CBR estimates, based on DCP tests in Test Section 6.

Depth* (mm/ in)	North	Middle	South
0/ 0	16	27	15
305/ 12	36	37	32
610/ 24	26	22	26
914/ 36	14	10	9

* Depth was measured from top of subgrade.

Table C7. CBR estimates, based on DCP tests in Test Section 7.

Depth* (mm/ in)	North	Middle	South
0/ 0	16	22	18
305/ 12	26	22	22
610/ 24	22	14	20
914/ 36	18	27	20

* Depth was measured from top of subgrade.

Table C8. CBR estimates, based on DCP tests in Test Section 8.

Depth* (mm/ in)	North	Middle	South
0/ 0	12	25	16
305/ 12	34	39	32
610/ 24	24	19	26
914/ 36	26	38	30

* Depth was measured from top of subgrade.

Table C9 DCP readings used to determine CBR estimates shown in Table C1.

Test Window 1, North		Test Window 1, Middle		Test Window 1, South	
Number of blows	Accumulative penetration (mm)	Number of blows	Accumulative penetration (mm)	Number of blows	Accumulative penetration (mm)
0	11	0	5	0	6
1	40	1	30	1	45
2	83	2	74	1	68
3	138	2	108	2	100
7	200	2	137	2	130
4	232	2	160	2	158
6	275	3	186	2	182
3	300	3	215	4	210
5	324	2	235	3	235
5	345	3	265	4	265
7	385	2	285	3	291
5	420	3	304	4	318
4	452	4	329	5	340
4	482	4	354	6	366
4	505	4	384	5	401
4	525	4	420	4	428
4	550	4	461	4	450
4	572	3	482	6	480
4	602	3	501	6	511
4	628	3	521	6	555
4	655	4	552	4	591
4	675	4	586	4	638
4	691	4	623	4	677
6	718	4	670	4	705
4	742	2	687	4	732
4	771	2	699	6	765
4	812	3	717	6	803
1	825	4	738	4	828
2	853	3	756	4	865
2	891	4	783	6	930
1	915	4	818	0	6
1	942	3	849	1	45
0	11	3	890	1	68
1	40	2	923	2	100
2	83	0	5	2	130
3	138	1	30	2	158
7	200	2	74	2	182
4	232	2	108	4	210
6	275	2	137	3	235
3	300	2	160	4	265
5	324	3	186	3	291
5	345	3	215	4	318
7	385	2	235	5	340
5	420	3	265	6	366
4	452	2	285	5	401
		3	304	4	428
		4	329		

Table C10 DCP readings used to determine CBR estimates shown in Table C2.

Test Window 2, North		Test Window 2, Middle		Test Window 2, South	
Number of blows	Accumulative penetration (mm)	Number of blows	Accumulative penetration (mm)	Number of blows	Accumulative penetration (mm)
0	10	0	7	0	5
1	45	1	48	1	42
1	66	1	70	1	64
1	85	2	101	1	83
2	114	2	131	2	118
2	137	2	154	2	143
2	160	2	177	2	176
2	182	2	203	2	201
4	221	2	223	2	228
3	240	2	239	2	245
4	264	2	251	2	263
4	292	4	275	5	292
4	317	3	293	5	325
4	346	7	337	5	357
4	370	6	355	5	383
4	392	6	378	5	412
6	415	6	397	5	444
5	439	6	418	4	465
7	470	6	450	4	489
4	497	6	481	4	508
4	522	6	507	4	522
7	560	6	532	6	556
4	583	6	558	6	583
4	608	6	593	6	633
4	645	4	625	4	676
4	695	4	662	4	733
4	751	4	695	4	782
3	769	4	718	3	799
5	795	4	738	3	814
7	832	4	760	4	830
4	854	6	789	5	858
2	873	4	815	5	893
3	896	4	845	2	914
2	918	4	885		
		3	919		

Table C11. DCP readings used to determine CBR estimates shown in Table C3.

Test Window 3, North		Test Window 3, Middle		Test Window 3, South	
Number of blows	Accumulative penetration (mm)	Number of blows	Accumulative penetration (mm)	Number of blows	Accumulative penetration (mm)
0	6	0	7	0	7
1	49	1	36	1	58
1	76	1	55	1	85
1	96	1	74	1	106
2	127	2	110	1	121
2	155	2	142	2	145
2	180	3	172	2	165
3	209	4	200	2	183
3	230	4	227	2	203
3	251	4	255	2	220
4	280	4	278	4	248
4	311	5	305	4	271
4	337	4	327	4	293
5	367	4	352	5	318
5	397	4	378	5	345
5	428	5	409	4	366
5	457	5	433	5	388
7	489	5	460	5	413
5	518	5	492	5	442
4	553	5	527	5	474
5	600	5	570	5	511
3	636	3	597	5	558
2	661	3	635	5	613
3	692	3	674	3	661
3	722	3	701	3	687
3	744	3	725	3	703
3	762	3	742	4	723
5	793	4	768	3	744
5	828	4	793	3	764
3	855	4	826	5	804
3	885	3	855	3	837
5	921	2	878	2	863
		2	892	1	876
		2	927	1	890
				1	905
				1	924

Table C12. DCP readings used to determine CBR estimates shown in Table C4.

Test Window 4, North		Test Window 4, Middle		Test Window 4, South	
Number of blows	Accumulative penetration (mm)	Number of blows	Accumulative penetration (mm)	Number of blows	Accumulative penetration (mm)
0	4	0	4	0	10
1	36	1	39	1	51
2	72	1	67	1	76
2	105	1	86	1	97
2	133	1	102	2	132
2	160	2	135	2	158
2	186	2	164	3	188
2	217	2	193	3	206
2	236	2	221	3	227
2	258	2	247	3	251
3	280	2	265	4	228
6	312	4	288	4	298
4	336	4	310	4	322
5	365	6	340	4	344
5	392	6	365	6	377
5	417	6	392	6	415
5	439	6	420	5	447
5	463	6	452	7	468
10	510	6	483	7	504
7	533	6	509	7	539
7	562	6	536	7	588
7	595	6	573	3	625
7	638	6	619	3	658
7	695	6	682	3	684
7	758	4	718	3	703
5	781	4	742	5	728
5	804	4	765	5	757
7	833	4	788	5	777
7	867	4	812	5	815
5	906	4	837	5	856
		5	877	5	907
		3	906	3	953
		2	925		

Table C13. DCP readings used to determine CBR estimates shown in Table C5.

Test Window 5, North		Test Window 5, Middle		Test Window 5, South	
Number of blows	Accumulative penetration (mm)	Number of blows	Accumulative penetration (mm)	Number of blows	Accumulative penetration (mm)
0	4	0	4	0	10
1	36	1	39	1	51
2	72	1	67	1	76
2	105	1	86	1	97
2	133	1	102	2	132
2	160	2	135	2	158
2	186	2	164	3	188
2	217	2	193	3	206
2	236	2	221	3	227
2	258	2	247	3	251
3	280	2	265	4	228
6	312	4	288	4	298
4	336	4	310	4	322
5	365	6	340	4	344
5	392	6	365	6	377
5	417	6	392	6	415
5	439	6	420	5	447
5	463	6	452	7	468
10	510	6	483	7	504
7	533	6	509	7	539
7	562	6	536	7	588
7	595	6	573	3	625
7	638	6	619	3	658
7	695	6	682	3	684
7	758	4	718	3	703
5	781	4	742	5	728
5	804	4	765	5	757
7	833	4	788	5	777
7	867	4	812	5	815
5	906	4	837	5	856
		5	877	5	907
		3	906	3	953
		2	925		

Table C14. DCP readings used to determine CBR estimates shown in Table C6.

Test Window 6, North		Test Window 6, Middle		Test Window 6, South	
Number of blows	Accumulative penetration (mm)	Number of blows	Accumulative penetration (mm)	Number of blows	Accumulative penetration (mm)
0	0	0	0	0	0
2	35	2	35	1	25
3	65	3	65	3	55
4	98	3	90	3	80
3	125	3	115	3	105
2	150	3	140	4	135
2	175	3	170	4	170
3	200	3	200	4	210
5	230	3	225	3	240
5	255	4	250	3	265
5	280	5	275	5	290
4	305	5	300	5	320
3	330	4	325	5	345
3	355	3	350	5	370
3	385	3	375	6	395
3	410	3	400	5	420
4	435	4	450	5	445
4	460	5	480	4	470
5	485	4	505	4	500
5	510	4	530	3	525
5	540	4	560	3	555
4	570	3	585	3	590
4	605	3	615	3	630
4	650	2	640	2	660
2	675	2	670	2	695
2	705	2	702	2	735
2	735	2	740	2	780
2	770	2	775	1	805
2	810	2	810	1	830
1	835	2	850	1	855
1	865	1	875	1	880
1	895	2	915	3	905
1	925			3	930

Table C15. DCP readings used to determine CBR estimates shown in Table C7.

Test Window 7, North		Test Window 7, Middle		Test Window 7, South	
Number of blows	Accumulative penetration (mm)	Number of blows	Accumulative penetration (mm)	Number of blows	Accumulative penetration (mm)
0	5	0	10	0	5
1	30	2	35	1	30
2	55	4	70	2	55
2	80	3	96	2	80
2	110	3	125	2	105
2	135	3	155	2	135
2	165	3	185	3	175
2	190	3	210	2	202
5	225	4	240	5	233
6	250	4	275	5	260
4	280	3	305	4	290
4	310	2	330	3	315
4	335	3	365	3	345
5	360	3	395	3	370
4	385	3	420	3	395
4	415	4	450	4	423
3	445	3	475	4	450
3	480	4	505	4	480
1	505	3	535	4	505
2	535	2	560	4	533
2	565	1	585	4	565
2	605	2	615	3	590
1	630	2	650	2	615
1	660	2	685	3	650
1	695	2	723	2	680
1	720	2	755	2	710
1	750	3	785	2	735
2	790	4	815	3	765
3	815	4	840	5	790
8	840	4	865	6	815
7	865	5	890	8	845
9	890	3	915	5	870
7	915			5	895
				5	920

Table C16. DCP readings used to determine CBR estimates shown in Table C8.

Test Window 8, North		Test Window 8, Middle		Test Window 8, South	
Number of blows	Accumulative penetration (mm)	Number of blows	Accumulative penetration (mm)	Number of blows	Accumulative penetration (mm)
0	0	0	5	0	10
2	35	2	40	3	40
2	60	2	70	4	70
3	90	3	95	4	100
4	120	3	123	3	130
3	145	3	150	3	160
3	175	3	180	3	190
3	205	2	205	4	215
3	235	3	235	3	238
4	264	5	265	4	265
5	290	5	290	4	290
5	315	5	320	3	315
4	340	4	350	3	343
5	370	3	375	3	370
4	395	4	400	3	400
6	420	4	428	4	425
6	445	4	445	4	450
6	470	4	480	4	475
5	500	4	505	5	500
4	525	4	535	5	525
3	550	4	568	4	550
3	580	3	600	5	580
3	615	3	635	5	610
2	640	3	665	3	635
2	670	2	700	3	660
2	710	2	740	3	688
2	750	2	790	3	715
1	780	1	815	4	740
1	805	2	853	5	765
1	830	2	878	8	790
2	860	4	905	8	820
3	890	4	930	8	845
4	915			9	870
				9	898
				14	925

The Clegg impact hammer is a 4.5 kg (10 lb) hammer is raised to a height of 457 mm (18 in) inside a guide tube, and dropped. A hand-held meter measures the peak deceleration as the hammer hits the surface. The deceleration is reported in tens of gravities and this unit is called Clegg IMPact Value (CIV). The percent CBR is determined from the following equation (Clegg, 1986):

$$CBR(\%) = (0.24(CIV) + 1)^2$$

For each test section, the percent CBR estimates obtained in this way at a location near the north end of the traffic window, at the middle, and near the south end of the traffic window are presented in Tables C10 through C19. Three drops were measured at each point, and the average of the three values was recorded.

Table C10. Clegg CBR on Test Section 1.

Location	Drop 1	Drop 2	Drop 3	Average
North	12	15	15	14
Middle	13	23	21	19
South	9	12	13	11

Table C11. Clegg CBR on Test Section 2.

Location	Drop 1	Drop 2	Drop 3	Average
North	10	15	15	13
Middle	6	10	12	9
South	10	13	15	13

Table C12. Clegg CBR on Test Section 3.

Location	Drop 1	Drop 2	Drop 3	Average
North	9	12	12	10
Middle	13	17	19	16
South	5	7	10	7

Table C13. Clegg CBR on Test Section 4.

Location	Drop 1	Drop 2	Drop 3	Average
North	10	13	15	13
Middle	10	13	15	13
South	6	9	12	9

Table C14. Clegg CBR on Test Section 5.

Location	Drop 1	Drop 2	Drop 3	Average
North	15	23	23	20
Middle	17	28	34	26
South	23	36	36	32

Table C15. Clegg CBR on Test Section 6.

Location	Drop 1	Drop 2	Drop 3	Average
North	15	23	26	21
Middle	13	19	19	17
South	15	23	26	21

Table C16. Clegg CBR on Test Section 7.

Location	Drop 1	Drop 2	Drop 3	Average
North	13	21	21	18
Middle	19	26	28	24
South	26	43	43	36

Table C17. Clegg CBR on Test Section 8.

Location	Drop 1	Drop 2	Drop 3	Average
North	15	19	19	18
Middle	13	19	19	17
South	12	21	26	19